

Complex Mixtures: Identifying and Characterizing Secondary Organic Aerosols

Emma Quinn Walhout

Grand Rapids, Michigan

Bachelor of Science in Chemistry,  
College of William & Mary, 2017

A Thesis presented to the Graduate Faculty of  
The College of William & Mary in Candidacy for the  
Degree of Master of Science

Department of Chemistry

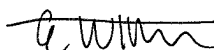
College of William & Mary  
May, 2019



## APPROVAL PAGE

This Thesis is submitted in partial fulfillment of  
the requirements for the degree of

Master of Science



---

Emma Quinn Walhout

Approved by the Committee May 2019



---

Committee Chair

Assistant Professor Rachel O'Brien, Chemistry  
College of William & Mary



---

Garrett-Robb-Guy Professor & Director of Undergraduate Studies  
John Poutsma, Chemistry  
College of William & Mary



---

Professor Lisa Landino, Chemistry  
College of William & Mary

## ABSTRACT

Complex organic mixtures in the environment can contain hundreds to thousands of different organic molecules, and their composition and reactivity can have important environmental implications. In addition to gases, the atmosphere is made of a variety of small liquids and solids called aerosols. These aerosols have large impacts on human health, climate, and atmospheric chemical reactions. Here, secondary organic aerosol (SOA) from the ozonolysis of  $\alpha$ -pinene is characterized. The atmospheric lifetime of SOA is very uncertain, but recent laboratory and modeling studies have demonstrated that photolysis is potentially an important process for organic mass loss from aerosol particles.<sup>1-5</sup> Photolysis modifies the molecular composition and properties of aerosols through photolytic cleaving and repartitioning of volatile products.

Characterization of dry, irradiated SOA can provide insights into photolysis driven changes in absorption properties and chemical composition. These results illuminate aging mechanisms and chemical and physical properties of organic aerosols in order to improve atmospheric modeling and the understanding of atmospheric chemical reactions. However, the high chemical complexity and low atmospheric abundance presents a difficult analytical challenge. Milligrams, or more, of material may be needed for speciated spectroscopic analysis.<sup>6</sup> This study used a suite of advanced analytical techniques, including a novel combination of action spectroscopy and mass spectrometry that provides more structural information on organic mixtures than mass spectrometry alone. This study also used tunable light from a free electron laser, infrared and UV/Vis absorption, and computational chemistry to characterize molecules in  $\alpha$ -pinene SOA.

In addition, complex organic mixtures are also found in particulate matter that has deposited onto Earth's surface. The preliminary results of dew analysis, including a foundation method of analysis for future study, gives the first look at organic material deposited into dew water on natural surfaces. This offers insight into atmospheric organic deposition to better understand chemical transport, air quality, and carbon cycling in the atmosphere.

# TABLE OF CONTENTS

Acknowledgements .....	iii
Dedication .....	iv
List of Tables .....	v
List of Figures .....	vi
Chapter 1: Introduction .....	1
1.1 Carbon in the Atmosphere .....	1
1.2 Aerosols in the Atmosphere .....	4
1.2.1 Direct and Indirect Radiative Forcing .....	7
1.3 Carbon and Aerosols' Effect and Impact.....	9
Motivation for Characterizing Complex, Atmospheric Organic Mixtures.....	11
Chapter 2: IRMPD Analysis at FELIX.....	16
2.1 Motivation for IRMPD Analysis .....	16
2.2 Instrumental and Computational Analysis.....	17
2.3 Experimental Methods .....	19
2.3.1 SOA Generation for IRMPD .....	19
2.3.2 Analysis at FELIX.....	21
2.4 Data Analysis and Discussion.....	22
2.4.1 Soft Ionization and Photodissociation .....	22
2.4.2 Comparison with Standards .....	23
2.4.3 Computational Analysis.....	25
2.4.4 Fragment Ion Spectra .....	26
Chapter 3: Atmospheric Aging of SOA through Photolysis.....	30
3.1 Motivation for SOA Photolysis .....	30
3.2 Experimental Methods .....	31
3.2.1 SOA Generation for Photolysis .....	31
3.2.2 Atmospheric Aging through Photolysis.....	33
3.2.3 ATR-FTIR Analysis: Investigating Changes in SOA Functional Groups .....	34
3.2.4 UV/Vis Analysis: Investigating the Change in Efficacy of SOA Absorption Properties.....	35
3.2.5 Mass Spectrometry Analysis: Determining SOA Concentration and Molecular Weight .....	36
3.3 Data Analysis and Discussion.....	37
3.3.1 Calculating Epsilon through Calibration Curves .....	37
3.3.2 Calculating and Analyzing the Cross Sections .....	41
3.3.3 ATR-FTIR Analysis .....	48
Chapter 4: Organic Deposition through Dew Analysis.....	57

4.1 Motivation for Investigating Organic Deposition .....	57
4.2 Experimental Methods .....	59
4.2.1 Materials and Collection Method .....	59
4.2.2 Preliminary Results .....	60
4.2.3 Future Research .....	63
Chapter 5: Conclusion .....	65
Appendix A .....	68
Appendix B .....	71
Appendix C .....	76
References .....	77

## ACKNOWLEDGEMENTS

First, I would like to thank Professor Rachel E. O'Brien for the opportunity to work in her lab, for her patience, guidance, insight, and leadership throughout my time as a graduate student. Thank you also to Professor John C. Poutsma, in whose class I discovered my love for analytics, and Professor Lisa Landino, whose inspiring teaching helped confirm my career choice in bioanalytics, for reviewing this manuscript and participating in my defense committee.

I would also like to thank my fellow research students and colleagues: members of the O'Brien Lab, especially Corey Thrasher and Jacob Shusterman.

I also want to express my gratitude to the donors who have made my twelve semesters at William & Mary possible. I would not have been able attend this amazing institution without their generosity. Lastly, I would like to acknowledge the Jeffress Memorial Trust Awards Program in Interdisciplinary Research, the Virginia Space Grant Consortium, and the William and Mary New Faculty Research Grant for funding. Thank you all.

Special thanks to my family and friends for supporting me through my program. A very special thanks to my Mimi for being the best editor anyone could hope for and for reading my thesis to the point of exhaustion. You are the best person I know. We don't appreciate you enough. Thank you to Maximillion for keeping me sane and always providing the softest shoulder to lie on, no matter how many walks were cut short.

## LIST OF TABLES

<b>Table 1</b> Summary of Fitted Peak Areas .....	55
<b>Table A1</b> IR Stretches for Calculated Lowest Energy Conformers.....	68
<b>Table B1</b> Summary of Preliminary SOA Filters .....	71
<b>Table B2</b> Summary of Dilutions for UV/Vis Analysis .....	72
<b>Table B3</b> Boxes with Zefluor Filters .....	72
<b>Table B4</b> Boxes with EZFlow Filters .....	73
<b>Table B5</b> Summary of Concentration Calculations for Box 1.1 .....	74
<b>Table B6</b> Summary of IR Stretches.....	75
<b>Table B7</b> Summary of Fitted Peak Areas Continued.....	75

## LIST OF FIGURES

<b>Figure 1</b> The Carbon Cycle.....	7
<b>Figure 2</b> IPCC Global Mean Radiative Forcing.....	8
<b>Figure 3</b> Composition of Aerosols from Various Global Locations.....	12
<b>Figure 4</b> Combined MS and IR Analysis Technique.....	17
<b>Figure 5</b> IRMPD SOA Generation Flow Tube.....	20
<b>Figure 6</b> IRMPD and Mass Spectra of Select SOA Monomers.....	22
<b>Figure 7</b> Experimental and Calculated Spectra of cis-Pinonic Acid.....	24
<b>Figure 8</b> Experimental and Calculated Spectra of 171 <i>m/z</i> .....	25
<b>Figure 9</b> Experimental and Calculated Spectra of 169 <i>m/z</i> .....	27
<b>Figure 10</b> Fragment Ion Spectra of 169 <i>m/z</i> .....	28
<b>Figure 11</b> Structure of $\alpha$ -pinene.....	31
<b>Figure 12</b> Photolysis SOA Generation Apparatus.....	32
<b>Figure 13</b> Photolysis Box.....	33
<b>Figure 14</b> Demonstrating Lamp Change Smoothing.....	40
<b>Figure 15</b> Calibration Curve at 310 nm.....	40
<b>Figure 16</b> Box 4 — Eliminating Position 4.....	41
<b>Figure 17</b> Comparing Position 4.....	42
<b>Figure 18</b> Comparing Box 1 to T0.....	43
<b>Figure 19</b> Comparing Light and Dark Boxes.....	44
<b>Figure 20</b> Absorbance of Zefluor and EZFlow Filters.....	45
<b>Figure 21</b> Comparing Box 1 and Box 6.....	46
<b>Figure 22</b> Determining SOA Loadings onto EZFlow Filters.....	47
<b>Figure 23</b> Absorbance of Box 6.....	47
<b>Figure 24</b> ATR-FTIR of Box 1.....	49
<b>Figure 25</b> Absorbance of Various SOA Loaded Filters.....	50
<b>Figure 26</b> Peak Picking of Box 1.1.....	50
<b>Figure 27</b> IR Carbonyl Peak for Light and Dark Boxes.....	52
<b>Figure 28</b> Comparing IR Shape Change After a Day of Photolysis.....	54
<b>Figure 29</b> Peak Picking of Light and Dark Boxes.....	54
<b>Figure 30</b> ATR-FTIR of Box 6.....	56
<b>Figure 31</b> ATR-FTIR of Zefluor and EZFlow Filters.....	56
<b>Figure 32</b> PPL Syringe.....	60
<b>Figure 33</b> AMS Mass Spectra of Dew and Lyophilized Dew Samples.....	61
<b>Figure 34</b> Mass Spectrum of Dew Sample.....	62
<b>Figure 35</b> FTICR Mass Spectrum of Dew Sample.....	62

## Chapter 1: Introduction

### 1.1 Carbon in the Atmosphere

The Earth's atmosphere is a dynamic system; it is the air we breathe and the environment in which we live. The composition and reactivity of trace atmospheric components directly affects living organisms, air quality, and climate change. Carbon is an essential trace element in the atmosphere and understanding its lifecycle is critical to understanding and predicting the effects of climate change. The collection of non-methane organic molecules, found in both volatile organic compounds (VOCs) and in organic aerosols, is called reactive organic carbon (ROC).<sup>7-9</sup> A great deal of work has been carried out to understand the composition of this material and the reactions it can undergo in the atmosphere as it plays a key role in driving the chemistry there and thus impacts ecosystems, climate change, and human health.<sup>9</sup>

A variety of sources deliver carbon into the atmosphere. These include anthropogenic emissions from human activities as well as natural, biogenic emissions from trees and plants. Carbon from anthropogenic sources, such as vehicle emissions, manufacturing, and waste incineration, is in the form of both VOCs and primary organic aerosol (POA). These VOCs can also react in the atmosphere to form secondary organic aerosol (SOA). The POA produced by these sources are finer particles formed from gas conversion and combustion.<sup>10,11</sup> Since the Industrial Revolution, humans have increased the amount of carbon emitted directly into the atmosphere. The contribution of these anthropogenic emissions, ~127 Tg/yr VOC,<sup>8</sup> is dominated by combustion of fossil

fuels.<sup>7,8,12</sup> Biogenic and natural emissions of carbon include volcanic eruptions, droplet spray and VOC emissions from rivers and oceans, forest fires and biomass burning, and wind erosion of rock faces<sup>10,13</sup> all of which generate larger particles that often contain elements from the soil.<sup>14</sup> But vegetation releases the largest quantity of VOCs, ~1,000 Tg/yr globally (isoprene ~50%; monoterpene ~15%; sesquiterpenes ~3%).<sup>7,8,12</sup>

The fate of atmospheric organic carbon (including carbon in the gas phase (VOCs) and in aerosol particles) is either complete oxidation to CO or CO<sub>2</sub>, or deposition (wet or dry).<sup>8</sup> On the path to either of these fates, organic molecules react in the atmosphere and are impacted by atmospheric aging. Their composition and structure can change via functionalization (oxidation) to form products with lower volatility (which can contribute to SOA) and fragmentation to form molecules of higher volatility.<sup>8</sup> Questions remain about the kinetics and products formed during these reactions as well as the total quantity of organic material removed via each pathway (CO<sub>2</sub> formation vs. deposition). One of the largest gaps lies in our understanding of the amount of SOA produced and the magnitude that is deposited out of the atmosphere.<sup>8</sup>

With the multitude of organic compounds present in the atmosphere, thousands of molecular structures exist. Molecular structure dictates an organic compound's properties, including location (gas vs. particle phase), and behavior in the atmosphere. For example, increased oxidation can add oxygen containing functional groups to a VOC molecule which decreases its vapor pressure and increases the likelihood it will condense onto aerosol or other surfaces. Organic

compounds greatly differ in fundamental properties like volatility, reactivity, water solubility, and cloud condensation nuclei (CCN) efficiency;<sup>8</sup> the fate of organic compounds, including their atmospheric lifecycles, lifetimes, and the impacts they have, depend on these structurally determined molecular properties. The volatility of a compound is very important<sup>8</sup> because it governs the partitioning between the gas and particle phases. Chemical reaction rates and removal rates differ between gas and particle phase molecules thus the location of the molecule (gas vs. particle) impacts the atmospheric lifetimes of compounds.<sup>8</sup>

Atmospheric lifetimes in the gas phase are based on reactivity and dependent upon the availability of radical oxidants and sunlight, while lifetimes in the particle phase are assumed to be longer because of lower formation rates of oxidants, shielding effects of neighboring compounds, and slow diffusion rates.<sup>8</sup> Organic compounds with low vapor pressures ( $<10^{-11}$  atm) tend to exist as aerosol particles while semi-volatile organic compounds (vapor pressures  $10^{-5}$  to  $10^{-11}$  atm) fluctuate between the gas and particle phase depending on surrounding temperature and pressure.<sup>8</sup>

Appreciating the complexity of ROC structures is vital to the comprehension of its reactions and properties and provides perspective for the impacts of SOA on atmospheric chemistry. By looking at the mixtures of chemicals in these condensed phases, we can probe the potential reactivity of the mixture in the atmosphere with important implications for organic carbon cycling.

This thesis focuses on studying carbon in the condensed phase. Two condensed phases exist in equilibrium with the gas phase on Earth. The first is aerosol particles, and the second is organic films deposited on Earth's surfaces through dry deposition of lower volatility VOC. Compounds in each phase are aged through oxidation, hydrolysis, or photolysis. Both phases are very complex mixtures of organic molecules with major questions remaining about their composition and how they react with the atmosphere; thus, advanced analytical techniques are needed to characterize these molecules.

## **1.2 Aerosols in the Atmosphere**

Atmospheric aerosols are made of a variety of liquid and solid particles suspended in the air.<sup>8,15</sup> Predictably, aerosols' compositions depend on their sources; for organic aerosols, these are the same anthropogenic and biogenic sources as carbon. Secondary aerosols, which are formed in the atmosphere, tend to be finer particles and are mostly composed of  $\text{SO}_4^{2-}$ ,  $\text{NO}_3^-$ , and  $\text{NH}_4^+$  from reactions of  $\text{SO}_2$ , nitrogen oxides, and  $\text{NH}_3$  found in the atmosphere.<sup>10,11</sup> Fine aerosol particles are less than 2  $\mu\text{m}$  in diameter.<sup>16</sup> In contrast, coarser particles range from 2 – 20  $\mu\text{m}$  in diameter.<sup>16</sup> Ninety percent of aerosols have natural origins, which generate these larger particles. There are about one million particles per cubic centimeter of anthropogenic aerosols and one thousand particles per cubic centimeter of naturally created aerosols.<sup>17</sup>

In 1995 it was estimated that one thousand to five thousand metric tons of soil dust a year contributed to atmospheric aerosols, and up to 50% of that was produced by human disturbances to the environment.<sup>11</sup> Organic aerosols make

up a significant portion of atmospheric fine particulate matter,<sup>18,19,20</sup> 20 – 90% of atmospheric dry particle mass.<sup>21</sup> These different sources mean aerosols consist of a myriad of compounds with varying physiochemical properties of which very little information is known.<sup>22,23,24</sup>

Given the range of different sources and particle types, classifications of aerosols are used to simplify the system. Aerosols are separated into two categories: primary and secondary aerosols.<sup>10</sup> Those characterized as primary aerosols are particles that have been directly emitted into the atmosphere as liquids or solids and exist in their original state.<sup>10,14,24,25</sup> Biomass burning; incomplete combustion of fossil fuels; volcanic eruptions; suspension of road, soil, and mineral dust; sea salt; and biological material such as plant fragments, microorganisms, and pollen all generate primary aerosols.<sup>24,25</sup>

SOA is formed in the atmosphere by gas-to-particle conversion.<sup>10,14,22,24</sup> VOCs are oxidized in the atmosphere initially forming a variety of alkyl, alkoxy, and peroxy radicals which, through either fragmentation or functionalization, transform into stable products like carbonyl compounds, carboxylic acids, and alcohols. Fragmentation leads to volatile products that can ultimately form CO<sub>2</sub> whereas most functionalization reactions create complex, lower volatility compounds which can condense into SOA.<sup>8</sup> Globally, biogenic VOCs account for around 90% of VOC emissions and of SOA formation at 90 billion kg of carbon a year.<sup>22</sup> However, there is an incomplete understanding of biogenic VOC contribution to the formation of SOA.<sup>7,8</sup>

Aerosols have different lifetimes spent in the atmosphere, from hours to weeks, making them very difficult to measure and categorize.<sup>16,17,26</sup> During their lifetimes, aerosols undergo various chemical and physical changes through processes summarized as atmospheric aging.<sup>24</sup> These transformations involve the changes in particle composition, size, structure through chemical reaction, and gas uptake.<sup>24</sup>

Organic aerosols are considered part of the carbon cycle (**Figure 1**<sup>17,27</sup>). Organic carbon enters the atmosphere at a rate of almost 1,000 Tg/yr. Once in the atmosphere, carbon can partition between the particle and gas phases. The distribution of semi-volatile organic compounds in these phases is important for understanding human toxicology and atmospheric chemistry.<sup>10</sup> Organic aerosol can be removed from the atmosphere and deposited back to Earth's surface as either wet or dry deposition. Wet deposition occurs when particles reach the surface of the earth as a result of precipitation.<sup>24</sup> Dry deposition occurs when aerosols are removed without the aid of airborne water particles or precipitation.<sup>24</sup> There is a chance, after deposition, for these particles to be re-emitted into the atmosphere, represented by the dashed line in Figure 1, but quantitative data is uncertain. The other loss process of organic carbon from the VOC/aerosol mixture is through complete oxidation to CO and CO<sub>2</sub>.<sup>17</sup>

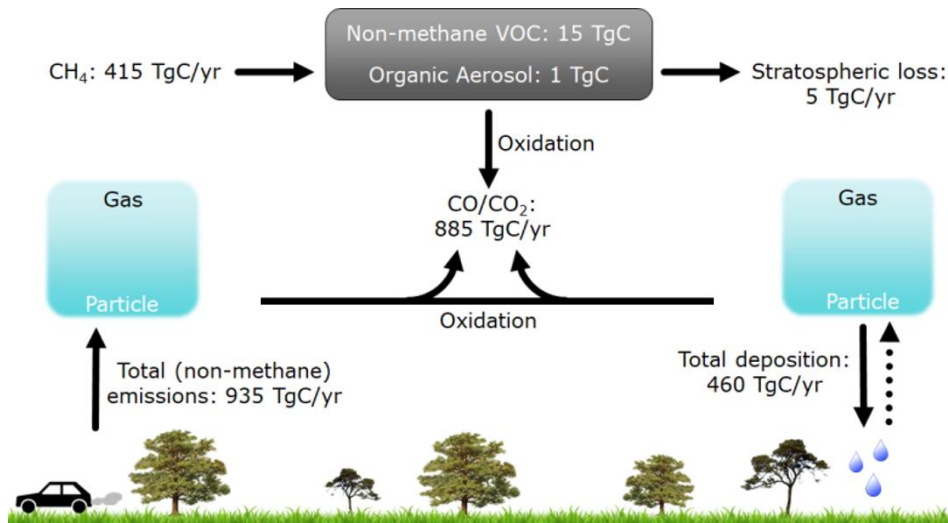


**Figure 1** The carbon cycle. The dashed arrow indicates a path of re-emission.

### 1.2.1 Direct and Indirect Radiative Forcing

The earth exists within a balance of incoming solar radiation and outgoing infrared radiation; this energy balance is known as the radiative forcing budget, and it affects the temperature of the earth.<sup>23,28,29</sup> There are two types of radiative forcing — positive and negative.<sup>28,29</sup> Positive radiative forcing increases the energy budget and leads to warming by agents absorbing infrared radiation and re-emitting it back to Earth's surface.<sup>10,23</sup> Negative radiative forcing decreases the energy budget leading to cooling by agents reflecting solar radiation back into space.<sup>10</sup> Carbon plays a role in the radiative budget, as do aerosols. Aerosols have the capability to affect both positive and negative radiative forcing, directly and indirectly,<sup>10,15,28</sup> but the extent of their effects is largely unknown (**Figure 2**<sup>11,16,30</sup>).

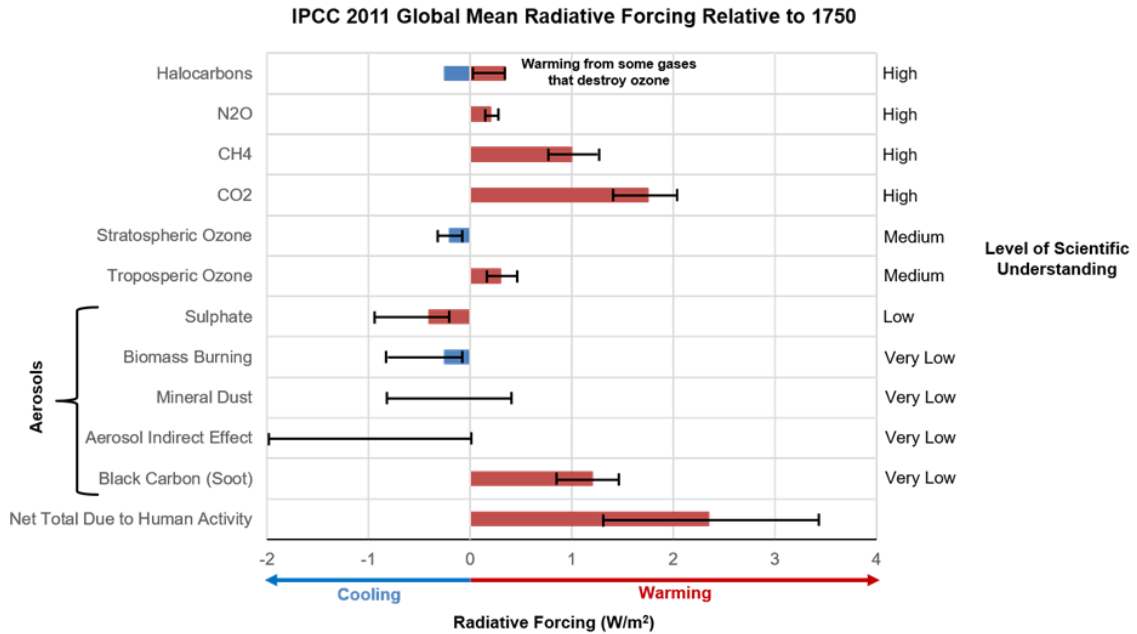


**Figure 2** The Global Mean Radiative Forcing Budget.

Aerosols directly contribute to radiative forcing by both scattering and absorbing these two types of incoming and outgoing radiation.<sup>11,13,16,22</sup> Scattering occurs when a particle changes the direction of propagation of a radiation beam — without an absorption taking place — through reflection, refraction, or diffraction.<sup>16,22</sup> The efficacy of a particle’s scattering depends on size; the larger the particle, the more efficient scattering. Atmospheric aerosols with a diameter between 0.1 and 1  $\mu\text{m}$  can accumulate<sup>23</sup> in the atmosphere due to their inefficient removal mechanisms and become efficient scatterers of solar radiation.<sup>16</sup> Maximum scattering is achieved for a particle, or particle cluster from accumulation, with a radius corresponding to the wavelength of radiation.<sup>16</sup> Light scattering can be measured and calculated from definitive aerosol size and composition.<sup>11</sup>

Aerosols act as an indirect agent by altering cloud formation, cloud properties, and precipitation efficiency.<sup>11,16</sup> When aerosols take on the role of

CCN, small particles providing a surface on which water vapor can condense, they form what can be called “polluted” clouds.<sup>11,16,17</sup> Polluted air contains a higher concentration of water soluble particles; therefore, pollution rich clouds have more numerous but smaller droplets making the cloud look brighter than it otherwise might be. The many droplets provide more surface area for reflection thus scattering more light and sending radiation back into space, producing net cooling.<sup>16</sup> This cloud albedo effect is poorly characterized and has only recently started to be quantified.<sup>7,8,13</sup> These polluted clouds spend a longer time in the atmosphere, produce a smaller droplet number concentration (produce less rain), and reflect more light away from the earth’s surface.<sup>10,11,17</sup> Polar functional groups such as carboxylic and dicarboxylic acids contribute to organic aerosols’ water solubility thus making them excellent candidates as CCN.<sup>11</sup>

Models estimate aerosols’ cooling effect has counteracted only about half of the warming caused by the buildup of greenhouse gases since the 1880s, yet scientists believe the cooling from reflective aerosols, including sulfates, overwhelms the warming facilitated by black carbon and other absorbing aerosols over the planet.<sup>13</sup> However, unlike most greenhouse gases, aerosols are not distributed evenly around the planet, so their impacts are more strongly felt regionally.<sup>13</sup>

### **1.3 Carbon and Aerosols’ Effect and Impact**

Aerosols’ concentration, size, asymmetrical shape, mass, phase, chemical composition, lifetime, and surface properties — all of which are highly variable spatially and temporally — have unquantified impacts on radiative forcing, human

health, ecosystems, regional visibility, global transportation, and deposition.<sup>10,19,20,23,24,31,32</sup>

It has been well established that exposure to aerosols has damaging effects on respiratory and cardiovascular systems.<sup>14,16,23</sup> Aerosol size and solubility play a major role in determining whether particles can be inhaled (and therefore, absorbed) into an organism's respiratory system.<sup>10</sup> Smaller particles have the ability to penetrate deeper into the lungs where the body has no way to dispose of them.<sup>10</sup> This type of aerosol exposure increases the risk of pneumonia, lung cancer, and heart disease and contributes to about four million premature deaths per year worldwide.<sup>17</sup>

Atmospheric particulate matter has a strong, yet poorly characterized effect on climate.<sup>21,33</sup> It's no secret that Earth's temperature, as a whole, has been rising over the last 100 years.<sup>29,34</sup> CO<sub>2</sub> levels have been creeping up since the first measurement in 1958;<sup>35,36</sup> in fact, only 10 years later, in 1968, CO<sub>2</sub> levels had increased by 8 ppm.<sup>35-38</sup> Arguably, the influence from aerosols most talked about is their contribution to climate change. The haze over a cityscape is a clear indication of the impact of aerosols on climate.<sup>19,20,31,32</sup> The ability to see objects over far distances depends on the concentration of aerosols and their absorbance and light scattering characteristics within that distance.<sup>10,16</sup> An absence of aerosols, and their scattering ability, would increase visible range to about 186 miles.<sup>16</sup>

Additionally, aerosols can be carried over long distances; accumulation also facilitates this transportation.<sup>13,23</sup> Particles move with the atmosphere at 5

m/s and travel thousands of miles in a week.<sup>13</sup> In fact, mineral dust that originated in western China has been detected in western North America and mineral dust from Africa has been found in Florida.<sup>10</sup> Looking at organic aerosols from polluted regions provides understanding of aerosol distribution and regional anthropogenic and natural sources of aerosol particles.

The uncertainty in aerosols' contribution to the radiative forcing budget, and the impacts had on human health and Earth's climate, need to be explored.<sup>16,30</sup>

#### **1.4 Motivation for Characterizing Complex, Atmospheric Organic Mixtures**

To decisively know aerosols' complete, quantitative contribution to the radiative balance, a clear distinction must be made between anthropogenic and natural aerosols.<sup>11</sup> Additionally, spatially and temporally resolved information, the radiative properties aerosols possess, and further understanding of aerosol size variance — including any changes due to relative humidity (solubility) and refractive index — needs to be reasonably determined.<sup>11</sup> Gaining insight into the contents of the atmosphere and the reactions that take place within it can lead to improved health, reduced (and possibly partially reverse) impact to climate change, and a greater understanding of chemistry as a whole. With better understanding comes better prevention and control.

Quantitative and predictive understanding of aerosols, particularly SOA, are extremely limited, and this incomplete understanding of aerosols' properties, such as their specific sources and quantities released by those sources, their composition and mechanisms of formation, and full scope of their direct and

indirect contribution to the global energy budget, is a driving force for current aerosol study.<sup>14</sup>

Particle mass spectrometry measurements taken from a variety of ground-based monitoring locations, and from aircrafts, show most particles dispersed throughout the troposphere are organics — anywhere from ten to one hundred thousand different organic compounds (**Figure 3**<sup>14,19</sup>).

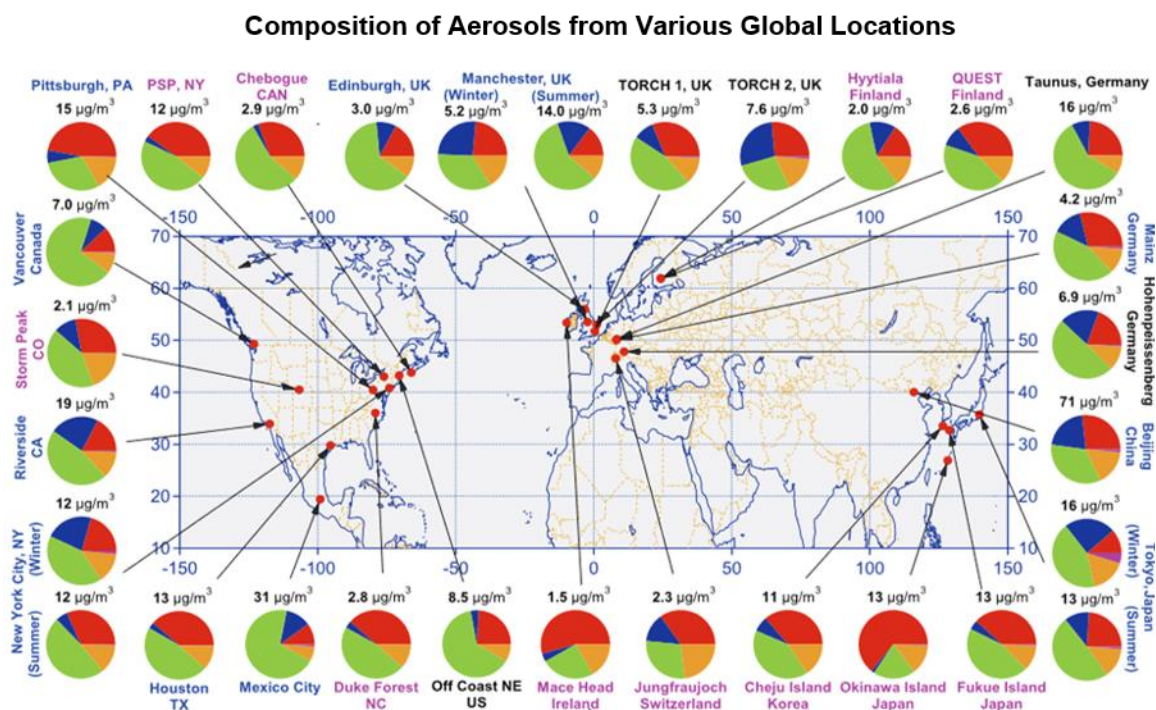


**Figure 3** Locations of AMS datasets. Study labels indicate the type of sample location: urban area (blue), <100mi. downwind of major cities (black), and rural areas >100mi. downwind (pink). Pie charts show the average mass concentration and chemical composition: organics (green), sulfate (red), nitrate (blue), ammonium (orange), and chloride (purple) of non-refractory, submicron aerosols.

Yet the bulk of atmospheric research and understanding is of inorganic ions and small acids. There is a comprehensive understanding through research and measurement of inorganic gas conversion such as sulfur dioxide, nitrate, and ammonium, but much ambiguity when it comes to SOA formation from oxidation

products of VOCs undergoing gas-particle transfer.<sup>14</sup> VOC reaction with hydroxyl radicals, ozone, nitrate radicals, or via photolysis cause VOC oxidation and the formation of organic products with polar, oxygenated functional groups.<sup>14</sup> Not only are these products water soluble, but they are also less volatile,<sup>14</sup> which contributes to their longer lifetimes in the atmosphere and the ability to form SOA.

To get estimates of global SOA production, two approaches are used: 1) bottom-up or 2) top-down. The bottom-up technique is the most traditional approach where known or inferred biogenic VOCs, such as isoprene and terpene, or anthropogenic VOC precursors, are combined in a global model built from oxidation experiments leading to SOA formations. It gives a global organic aerosol estimation.<sup>14</sup> The top-down method estimates SOA distribution in the atmosphere by inferring global SOA production based on known precursor emissions.<sup>14,29</sup> It is essential to have correct computer models for environmental predictions, yet when it comes to predicting and accounting for aerosols, there is much room for improvement. VOC mass loadings and SOA formation and lifelong characteristics are severely underestimated in current models.<sup>8,21,39,40</sup>

Only a handful of the 25 climate models considered by the Fourth Intergovernmental Panel on Climate Change (IPCC) considered the direct effects of aerosols other than sulfates, and fewer than a third of the models included, even in a very limited way, indirect aerosol effects.<sup>13</sup> One of the most significant fundamental assumptions current gas particle partitioning models maintain is that SOA particles remain in a liquid state throughout their lifetime in the atmosphere

and therefore SOA evaporates with the same kinetics as a liquid droplet and that this evaporation behavior is size dependent.<sup>14,21,41,42</sup> This affects calculations of condensation and evaporation of particles in the atmosphere.<sup>14,21,41,42</sup> But research has shown SOA particles are not just liquid throughout their lifetime; for example, SOA has been presented as solid under ambient conditions, and consequently do not behave as expected.<sup>21,22,43</sup> Organic compounds can re-evaporate back into the atmosphere over hours or days, much longer than the calculated minutes from evaporation kinetics.<sup>8</sup> Experimental findings regarding SOA phase, evaporation rates, aging, etc. indicate the need to reformulate the way SOA is treated by models.<sup>21</sup>

Through analysis including an aerosol mass spectrometer (AMS), an Orbitrap™ MS, attenuated total reflectance Fourier transform infrared spectrometer (ATR-FTIR), UV/Vis spectrometer, and computational analysis, the William and Mary O'Brien lab characterizes SOA in order to 1) understand the chemical and physical properties of SOA as they naturally age to determine how these products behave in the atmosphere which will allow us to more accurately predict their impacts and improve models and 2) understand, quantitatively, how influential these SOA are on the environment and health. The specific impacts my research has had and will have in this overall goal is the development of analytical techniques and experimental platforms to build a foundational framework for investigating complex organic mixtures in the atmosphere by looking at aerosol composition through mass spectrometry and computations;

aerosol lifetimes and natural aging through photolysis, IR, and UV/Vis; and analyzing material found in dew as a proxy for gas phase deposition.

## Chapter 2: IRMPD Analysis at FELIX

### 2.1 Motivation for IRMPD Analysis

SOA is highly chemically complex with low atmospheric abundance which makes it difficult to analyze; spectroscopic analysis needs milligrams or more of material to speciate molecules. Mass spectrometry has high sensitivity (able to deal with trace samples) and high mass resolving power (able to observe the rapid chemical reactions that are occurring) but comes at the expense of structural information.<sup>44-50</sup> Previous studies have coupled mass spectrometry with online derivatization,<sup>51,52</sup> two-dimensional gas chromatography,<sup>53</sup> liquid chromatography,<sup>54</sup> and ion mobility separations<sup>55</sup> to expand the range of SOA compounds that are separated and characterized, yet gaps remain in the ability to fully speciate organic mixtures. Mass spectrometry, alone, is unable to resolve isomers which are often present in complex organic mixtures.

Infrared (IR) action spectroscopy of gas phase ions provides spectra similar to IR absorption spectroscopy. When combined, mass spectrometry and IR techniques make up for the shortcomings of the other by uniting the information obtained from fingerprint IR spectroscopy and mass spectrometry to generate characteristic IR spectra of individual isolated ion populations. **Figure 4** shows a simplified diagram of this combined analysis. Individual ions are isolated in the mass spectrometer, a mass to charge ratio is isolated and irradiated, and then scanned to generate an IR spectrum. Soft ionization combined with in-situ IR, using the tunable free-electron laser at FELIX, provides detailed information on molecular structures and functional groups.

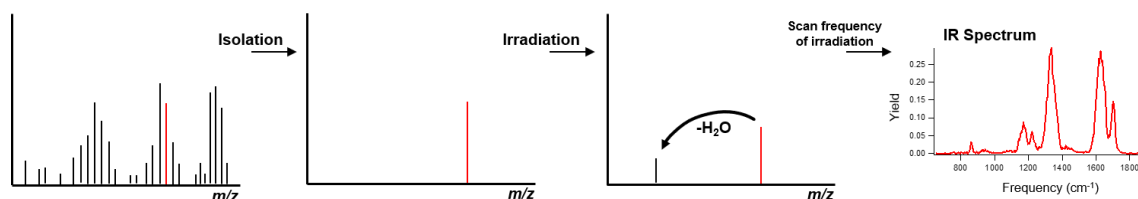


**Figure 4** The combined MS and IR analysis technique following the collection of aerosols.

Applying this novel analytical technique of merging the strengths of IR action spectroscopy with mass spectrometry, along with computational modeling, characterizes organic molecules in SOA, formed from the ozonolysis of  $\alpha$ -pinene. The results of a good spectral overlap between 1) a standard and an expected, first generation SOA, thus identifying the molecular structure of the ion, and 2) the characterization of isomers for multiple SOA products, using both computations and analyses of fragment ion spectra, demonstrate the detailed structural information obtained by this combination of analytical techniques. While acceptable spectral matches between standards and unknowns do not necessarily positively identify the structure of an unknown, this technique provides a solid support for assignments, especially if known isomers have differing IRMPD spectra. Even if the exact structure cannot be determined, the IRMPD spectrum will be able to significantly reduce the number of possible candidates.

## 2.2 Instrumental and Computational Analysis

Infrared multiphoton dissociation (IRMPD) is an action spectroscopy technique that fragments molecules in the gas phase. The resulting decrease in precursor ion signal and increase in fragment ion signal can be used to generate spectrum for structural analysis of the precursor molecule. (Action spectroscopy is the extent of photochemical reaction as a function of wavelength).<sup>56,57</sup> An IR

laser is directed through an IR transparent window into, for this particular experiment, a quadrupole ion trap MS (Bruker amaZon) to induce wavelength dependent photodissociation. The precursor molecule absorbs multiple IR photons until its bonds break from excited energetic vibrational states.

IR action spectroscopy of gas phase ions provides similar spectra to that of IR absorption spectroscopy; it probes ion dissociation after irradiation at specified wavelengths. IRMPD observes the fingerprint region ( $\sim 600 - 1900 \text{ cm}^{-1}$ ) or the hydrogen stretching region ( $2800 - 4000 \text{ cm}^{-1}$ ) using high intensity, tunable IR radiation, typically generated with free electron lasers (FEL) or optical parametric oscillator/amplifier (OPO/OPA) lasers, respectively.

The FEL in the FELIX Laboratory at Radboud University in Nijmegen, the Netherlands, was used to give detailed information on molecular structures and functional groups. This laser uses a combination of soft ionization with in situ IR spectroscopy.<sup>58</sup> FEL irradiated, mass-isolated ion populations in the MS produce data sets consisting of mass spectra showing the isolated precursor ion, the fragment ions produced as a function of IR wavelength, and the IRMPD spectrum of the selected ion.

Computational modeling aids in spectral interpretation of gas phase ion conformations.<sup>59-64</sup> Here, computational analysis is used to characterize isomers for multiple SOA products by comparing the computational ion spectra to that of the experimental IRMPD fragment ion spectra. Computations were carried out using PCModel 9.0 and Gaussian 09 software packages. Anions for each molecule were created by deprotonating at the most acidic site.

Each ion underwent manual, exhaustive conformational searches to locate all relevant structures. After ions were minimized in PCModel, the lowest energy conformers were searched for with the GMMX (Global-MMX) force field. Of the 10,000 conformers that were assessed, the four lowest free energy conformations of each ion were selected for further analysis.

Computations of ground state geometries and vibrational frequencies were calculated using density functional theory (DFT) at the B3LYP/6-311++G(d,p) level of theory with Gaussian 09.<sup>65</sup> All computations were completed in the gas phase at 300 K to match experimental conditions. For these conformers, vibrational frequencies were extracted and adjusted by a scaling factor of 0.98.<sup>66</sup> Full width at half maximum of 20 cm<sup>-1</sup> was applied for easy comparison with experimental spectra.<sup>67</sup>

## **2.3 Experimental Methods**

### **2.3.1 SOA Generation for IRMPD**

The sample preparation and data collection were carried out by Professor Rachel O'Brien at MIT and FELIX, respectively, as she was finishing her postdoctoral. The description below is provided by her; a similar type of SOA generation was conducted by me in the O'Brien laboratory at William and Mary and is described in Chapter 3.

Laboratory generated,  $\alpha$ -pinene SOA was collected on a filter, extracted, and characterized with IRMPD. Aerosols were generated in a five-foot long, 3 5/8 inch diameter polycarbonate flow tube (**Figure 5**).



**Figure 5** Polycarbonate flow tube for IRMPD SOA generation.

To create a laminar flow region, a spacer with small holes was placed one foot away from the two inlets. The first inlet brought in zero air (Aadco 737-13 Pure Air Generator) at a flow rate of 1 L/min and had liquid  $\alpha$ -pinene (Sigma-Aldrich) evaporated into the airflow via a syringe pump (Harvard Apparatus) with a flow rate of 20  $\mu$ L/hr. The second inlet introduced 1.5 L/min of zero air from a Penray ozone generator (Model 600, Jelight Co. Inc.) which produced  $\sim$ 15 ppm ozone for the flow tube. The tube was at room temperature with ambient pressure, and the zero air source provided low relative humidity air (<5%).

After the aerosols were formed, they traveled through a four-foot black carbon denuder to remove excess ozone and VOCs before being collected on a Zefluor® 2.0  $\mu$ m Teflon™ filter. Collection was taken for three hours per filter at a flow rate of  $\sim$ 2 L/min; excess flow was vented through a carbon trap. Filters were weighed before and after collection to determine approximately 3 mg of sample was collected per filter. Filters were extracted in methanol (Sigma-Aldrich) and ultrasonicated for  $\sim$ 20 minutes; the extract was then dried using ultrapure nitrogen. Four filter extractions were combined, frozen, and transported to the FELIX Laboratory for analysis.

### 2.3.2 Analysis at FELIX

Analysis of samples at FELIX was conducted with the assistance of laboratory scientists at the facility. There, SOA extracts were diluted with 5 mL of a 50/50 water/methanol solution to a concentration of ~10 mM. Immediately before a run was taken, this stock SOA solution was further diluted, with methanol and ~0.1% ammonium hydroxide, to ~20 – 40  $\mu\text{M}$ ; this aided in ion formation for the negative ion mode.

The solution was passed into the instrument with a flow rate of 120  $\mu\text{L/hr}$ , spraying with a voltage of -4,500V, and dry  $\text{N}_2$  nebulizing gas. Precursor ions were isolated in the ion trap and irradiated for 2 – 3 seconds using the 10-Hz rep rate light pulses from the FEL. IRMPD yield, defined as the ratio of the summed fragment ion intensities divided by the total ion intensity, was determined from the recorded mass spectra. The IR frequency was scanned in steps of ~3  $\text{cm}^{-1}$ ; at each frequency in the fingerprint spectral region, new populations of ions were irradiated. An average of eight mass spectral scans were used for each irradiation wavelength, and IRMPD spectra were linearly corrected for variations in laser power as a function of photon energy.

The resulting data sets were brought to William and Mary by Professor O'Brien and given to me for analysis. The IRMPD spectra and fragmentation ion spectra were compared to previous work on  $\alpha$ -pinene SOA characterizations found in the literature, and computations were used to look for the presence of isomers.

## 2.4 Data Analysis and Discussion

### 2.4.1 Soft Ionization and Photodissociation

**Figure 6** shows an IRMPD spectrum of 157  $m/z$  (bottom) as a representative selected ion isolated from the full mass spectrum (top). Electrospray ionization (ESI) in the negative ion mode generated ions corresponding to monomers of  $\alpha$ -pinene ozonolysis products; dimers and trimers also formed through oligomerization reactions.<sup>68,69</sup> For this thesis, monomers that have previously been reported in the literature were the ions selected for isolation and irradiation. These include ion populations where both a single SOA product is expected as well as populations that should contain more than one isomer.

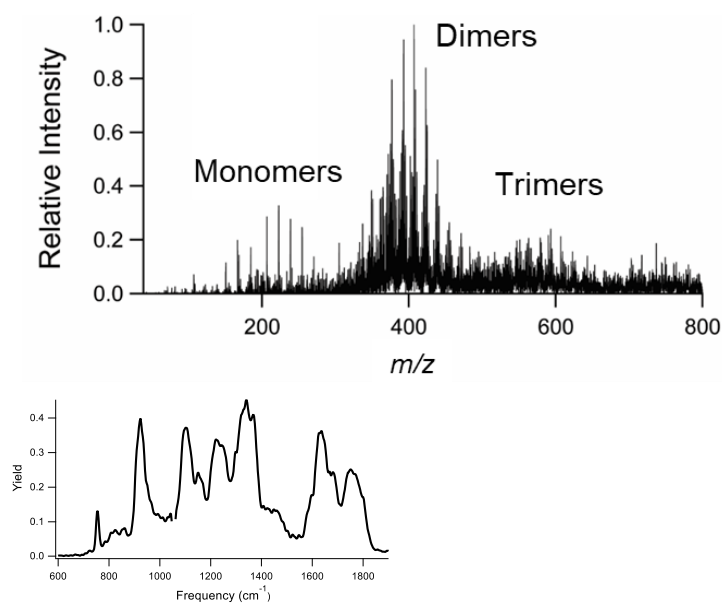


**Figure 6** IRMPD spectrum of a selected monomer ion (157  $m/z$ , bottom) from a full mass spectrum (top) of  $\alpha$ -pinene ozonolysis products.

The IRMPD spectra from the monomers show absorbance features in the carbonyl stretching region ( $\sim 1600 - 1800 \text{ cm}^{-1}$ , also seen in Figure 6) from the formation of ketones, aldehydes, carboxylic acids, and lactones during the ozonolysis reaction. A separate carbonyl peak can often be found at higher frequencies and, similar to absorption IR, this frequency can shift depending on whether the carbonyl is part of a ketone, aldehyde, or lactone functional group.<sup>70</sup> Additional peaks are observed at lower frequencies corresponding to other stretching modes and coupled vibrations. Computational comparisons deprotonate a carboxylic acid to form a carboxylate group with a distinct IR fingerprint characterized by both asymmetric and symmetric stretches.

The frequencies of the vibrations are very sensitive to the chemical environment. Thus, by comparing the location of these experimental absorption peaks to computations and/or standards, insights into the structure of the molecule can be gained. The full data sets obtained with this method contain information on molecular weight, tandem MS fragmentation products, and chemical structures of the isolated ion population. The following sections present a detailed characterization of select isolated mass to charge ratios to demonstrate the range and depth of information available with this technique.

#### **2.4.2 Comparison with Standards**

Comparing the IRMPD spectra of a known standard with an ion of the same expected identity, but formed from  $\alpha$ -pinene ozonolysis, demonstrates the utility of this technique to help identify the structure of unknowns using synthesized standards. Previous studies have determined that cis-Pinonic Acid is

a major SOA product.<sup>29,71,72</sup> The IRMPD spectra for the isolated, SOA anion at 183  $m/z$  and the standard cis-Pinonic Acid (Sigma-Aldrich), along with the computed IR spectrum of cis-Pinonic Acid, are compared in **Figure 7**.

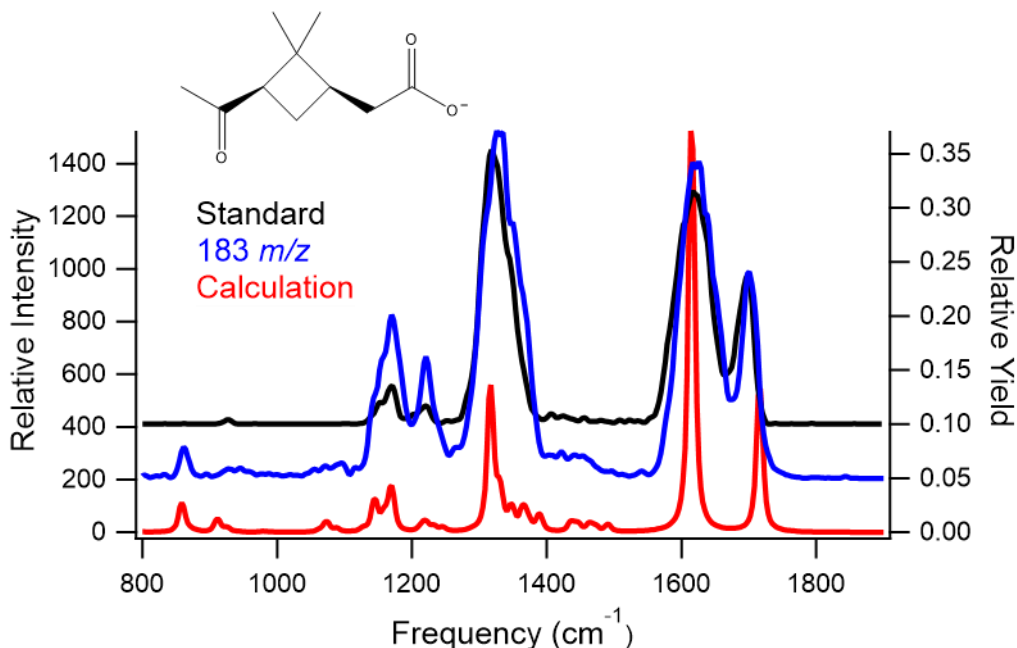


**Figure 7** The IRMPD spectra of standard cis-Pinonic Acid (black) and SOA ion 183  $m/z$  (blue), and calculated IR spectrum of cis-Pinonic Acid (red).

The high degree of overlap between the locations and relative intensities of the major absorption peaks confirm the identity of the SOA product. Assignments of IR absorption peaks can be made based on previous analyses of IRMPD spectra for molecules containing carboxylate and carbonyl groups<sup>67,73</sup> and quantum calculations. Peaks at 1617 and 1704  $\text{cm}^{-1}$  are associated with the asymmetric carboxylate stretch and the ketone carbonyl stretch, respectively; peak 1326  $\text{cm}^{-1}$  is the symmetric carboxylate stretch; and peaks at 1218 and 1170  $\text{cm}^{-1}$  are assigned to coupled CH vibrational modes. (A full collection of calculated SOA molecule observed stretches can be found in Appendix A).

### 2.4.3 Computational Analysis

When comparing experimental IRMPD spectra to computed spectra, the locations of the absorption peaks are most informative for structural interpretation. The intensities observed in the IRMPD spectra can be influenced by experimental factors, and DFT modeling of intensities is not as accurate as that of frequencies.<sup>60,63</sup> All calculated spectra presented here are of the lowest energy conformer.

The IRMPD spectrum for the ion population isolated at 171  $m/z$  (**Figure 8**) is very different from the one in Figure 7. This confirms the expectation that spectral differences can be observed between components in this mixture, despite the likely presence of similar functional groups in the product SOA molecules. The broader absorption peaks may be from contributions of multiple conformers or isomers but have also been observed when protons are shared between nucleophilic functional groups.<sup>67</sup>

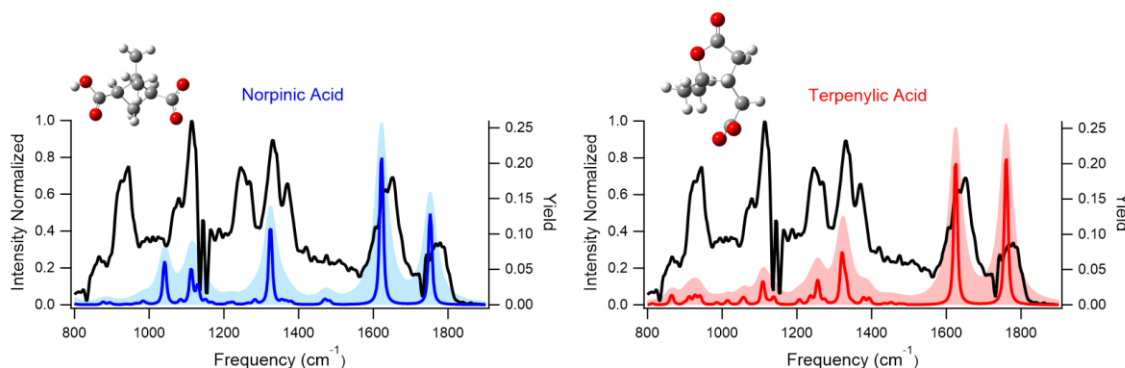


**Figure 8** Experimental IRMPD spectra for 171  $m/z$  (black) compared to the calculated spectra with 4  $\text{cm}^{-1}$  (colored line) and 20  $\text{cm}^{-1}$  (shaded) peak widths of Norpinic Acid (blue) and Terpenylic Acid (red).

The anion population with 171  $m/z$  has at least two potential isomers: Norpinic (blue) and Terpenylic (red) Acid.<sup>72,74,75</sup> For clarity of interpretation, the calculated spectra have been broadened by Gaussian peak convolution with

widths of 4 (colored line) and 20 (shaded)  $\text{cm}^{-1}$  full width at half maximum (FWHM). The calculated spectrum for Terpenylic Acid matches well with the experimental spectrum, especially for the major carbonyl ( $1780 \text{ cm}^{-1}$ ) and carboxylic acid ( $1644 \text{ cm}^{-1}$ ) C=O stretches.

Norpinic Acid's calculated spectrum somewhat matches the carbonyl peaks but is missing frequencies that correspond to the measured peaks near  $1250$  and  $930 \text{ cm}^{-1}$ . These missing calculated peaks indicate that Norpinic Acid may be present but cannot be the only isomer at  $171 m/z$ , thus making Terpenylic Acid the most likely candidate for this mass ratio.

#### 2.4.4 Fragment Ion Spectra

The IRMPD spectrum for  $169 m/z$ , shown in **Figure 9 A**, is very similar to the spectrum observed for  $183 m/z$ , cis-Pinonic Acid. Given this similarity, and the fact that a difference of 14 atomic mass units (amu) can be achieved by replacing a methyl group with a hydrogen, it is expected that possible structures for the dominant components are very similar to cis-Pinonic Acid. As previously reported, possible isomers of  $169 m/z$  include Pinalic-3-Acid, Pinalic-4-Acid, and Norpinonic Acid;<sup>29,76</sup> their calculated spectra are seen in Figure 9 B, C, and D, respectively.

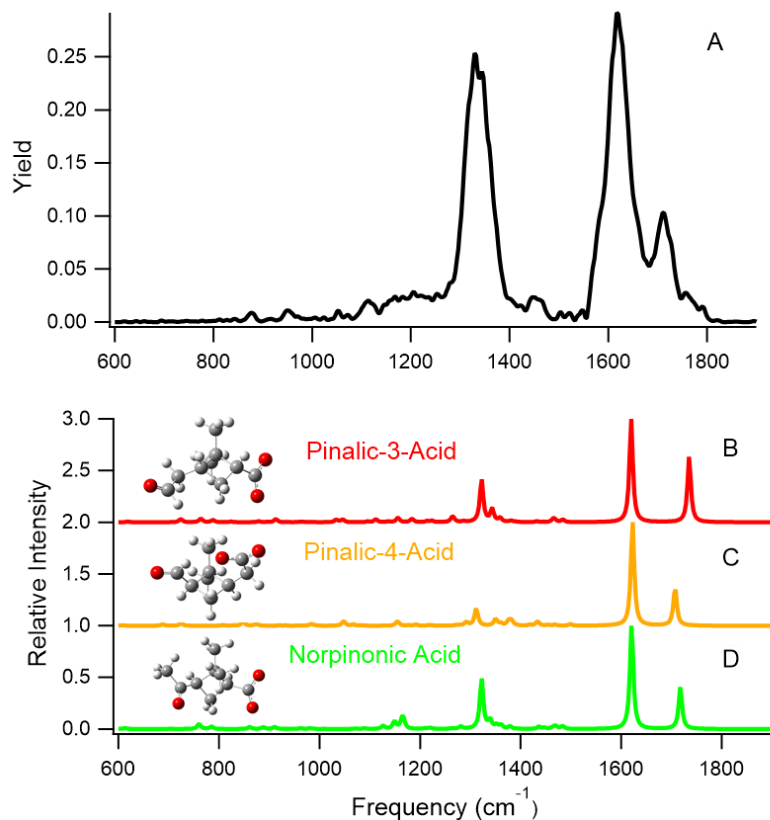


**Figure 9** (A) IRMPD spectrum for 169  $m/z$  and calculated spectra for (B) Pinalic-3-Acid, (C) Pinalic-4-Acid, and (D) Norpinonic Acid.

All three calculated spectra have two absorption peaks  $>1600\text{ cm}^{-1}$ . The lower peak ( $\sim 1620\text{ cm}^{-1}$ ) corresponds to the carboxylate asymmetric stretch in each isomer; the higher peak is the carbonyl stretch. This peak is calculated at  $1735$  and  $1720\text{ cm}^{-1}$  for Pinalic-3-Acid and Pinalic-4-Acid, respectively; both of which have an aldehyde functional group. Norpinonic Acid's higher peak is red-shifted to  $1695\text{ cm}^{-1}$ ; it has a ketone functional group. The absorption peak at  $\sim 1330\text{ cm}^{-1}$  corresponds to the symmetric carboxylate stretch. Because all three isomers have similar calculated spectra and the widths of the peaks in the experimental spectrum are relatively broad, chromatography combined with detailed scans of the regions with the largest calculated differences ( $\sim 1690 -$

1740  $\text{cm}^{-1}$  and 600 – 1200  $\text{cm}^{-1}$ ) would aid in the absolute identification of these compounds.

**Figure 10 A** shows the intensities of the IR-induced fragment ions averaged over the full IRMPD spectrum; the fragments are color coded to **Figure 10 C – G** which display the ions as a function of IR frequency. **Figure 10 B** is a reproduction of the IRMPD spectrum for the full ion population (**Figure 9 A**).

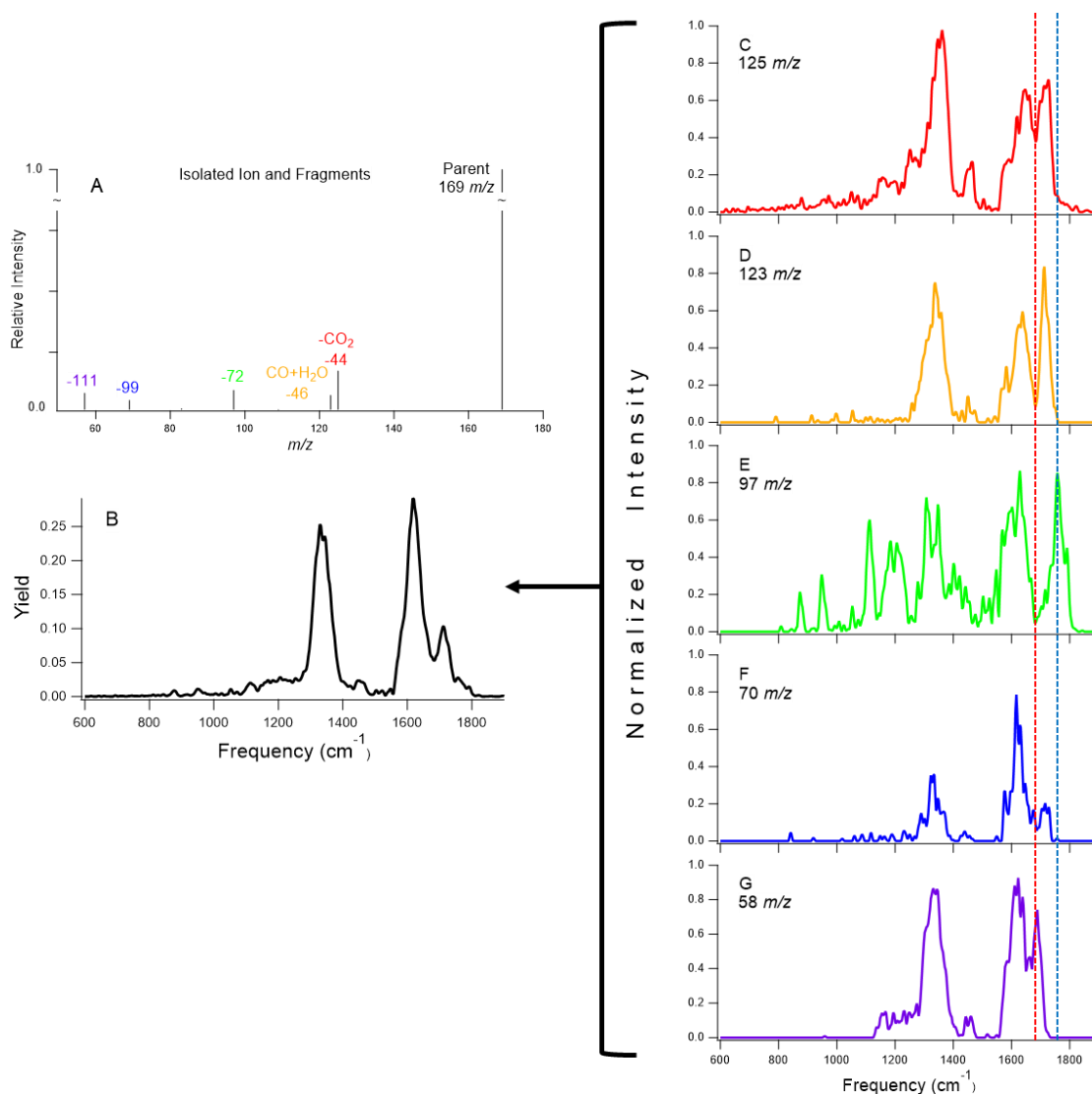


**Figure 10** Individual fragment ion spectra for the anion 169  $m/z$ . (A) Reconstructed fragment ion spectrum using the average intensity across the IRMPD scan. (B) IRMPD yield spectrum. (C – G) Fragment ion spectra. Vertical, dotted lines highlight the red-shifted (red) and blue-shifted (blue) peaks.

Fragment ions associated with the loss of CO<sub>2</sub> (-44 *m/z*, red) and CO with H<sub>2</sub>O (-46 *m/z*, orange) have very similar spectra, with the exception of the intensity difference for the peak near 1200 cm<sup>-1</sup>. Fragment ion 70 *m/z* (-99 neutral loss, blue) has similar peak locations but significant differences in intensities for the first two carbonyl stretch peaks (~1620 and 1715 cm<sup>-1</sup>). Fragment ion 58 *m/z* (-111 neutral loss, purple) also has an absorption peak ~1620 cm<sup>-1</sup>, but its higher carbonyl stretch peak is red-shifted to ~1686 cm<sup>-1</sup> compared to the red, orange, and blue fragment ions (vertical, red dashed line). These differences are consistent with the trend observed in Figure 9 where a red shift in peak position is present when the carbonyl is a ketone compared to an aldehyde.

Fragment ion 97 *m/z* (-72 neutral loss, green) has a carbonyl absorption peak centered around 1770 cm<sup>-1</sup>; a blue-shifted carbonyl stretch (vertical, blue dashed line). The DFT calculations for Pinalic-3-Acid, Pinalic-4-Acid, and Norpinonic Acid show no carbonyl stretching peaks near 1770 cm<sup>-1</sup> indicating fragment ion 97 *m/z* is possibly an unidentified isomer formed during α-pinene ozonolysis. Absorptions at 1780 cm<sup>-1</sup> have been observed for lactone containing molecules (like Terpenylic Acid) which suggests the structure for this isomer possibly contains a ketone on a ring providing similar electron density to that of a lactone functional group.

## **Chapter 3: Atmospheric Aging of SOA through Photolysis**

### **3.1 Motivation for SOA Photolysis**

To characterize chemical composition changes of dry SOA as a result of long-term atmospheric aging, with a focus on improving atmospheric modeling of SOA loss, SOA films undergoing photolysis were investigated. Photolytic aging leads to SOA mass loss and affected lifetimes in the atmosphere.<sup>5,77</sup> Because aerosols can chemically react they can fragment, therefore the sun could be destroying aerosol particles on a timescale much faster than is presently assumed. Currently, models are based on fresh SOA characteristics including their molecular composition and absorption cross sections. SOA is expected to degrade to the point of complete volatilization. However, photolytic aging bleaches the carbonyl chromophores, possibly decreasing the chemical changes that occur, causing SOA mass loadings to decay to a plateau rather than be completely destroyed. Much of the research of photochemical reactions occurring in the atmosphere has focused on photolysis of organics in water droplets. Though understanding how light affects organics in aqueous solutions helps us understand how the light from the sun affects the photochemical reactions of these mixtures in the atmosphere, aerosol particles spend a significant fraction of their lifetime dry. Thus, more research of ambient organics in the gas phase is needed to create a better proxy for atmospheric reactions.

After collection of SOA on filters and exposure to UV light over different lengths of time, changes were observed in the absorption cross sections of the sample with corresponding changes in the molecular composition characterized

with offline AMS and soft ionization ultrahigh resolution mass spectrometry (UHR-MS). The following presents advances in analytical techniques, a building of an experimental foundation being developed by this lab to enable a more thorough analysis of photolysis of complex SOA films.

## 3.2 Experimental and Methods

### 3.2.1 SOA Generation for Photolysis

The oxidation of various biogenic compounds produces SOA, but only terpenes are believed to be a significant source of SOA under atmospheric conditions;<sup>29</sup> monoterpenes are considered the most reactive of these compounds.<sup>29</sup>  $\alpha$ -pinene, a naturally emitted molecule from pine trees and the most abundant biogenic monoterpene,<sup>7,23</sup> is

unsaturated and can be rapidly oxidized by ozone, OH radicals, and  $\text{NO}_3$  radicals.<sup>29</sup> A majority of the observed aerosol products come from the reaction of  $\alpha$ -pinene and

ozone,<sup>20,21,24,29</sup> one of the most abundant oxidants in Earth's atmosphere.<sup>16</sup>

Laboratory generated SOA, including the aerosols observed for this thesis with lifetimes of about 1 – 2 weeks, exhibit evaporation behavior quite similar to that of ambient SOA<sup>21</sup> making them perfectly acceptable as a proxy for SOA aging processes happening in the atmosphere.

A similar SOA generating apparatus to the one described in the previous chapter was developed (**Figure 12**).

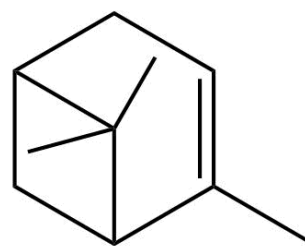


**Figure 11**  $\alpha$ -pinene structure.

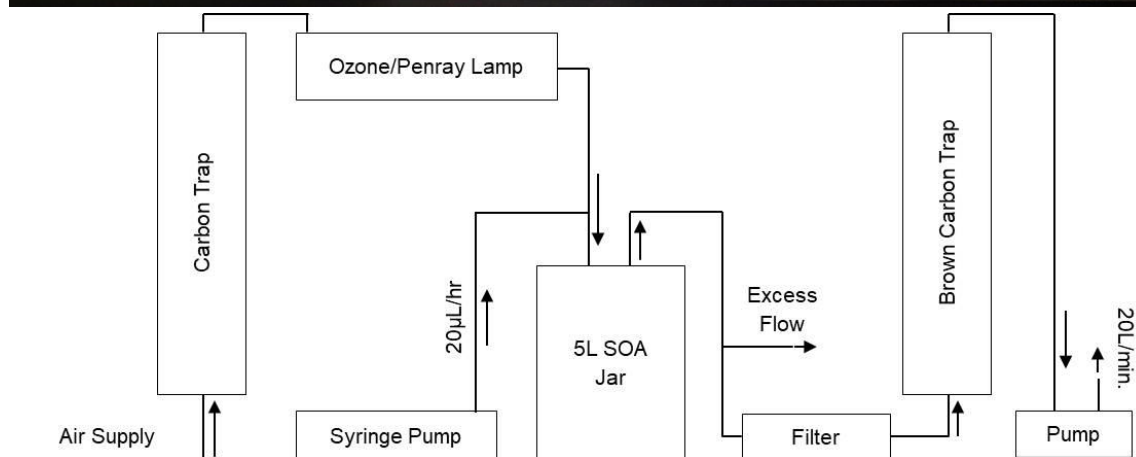
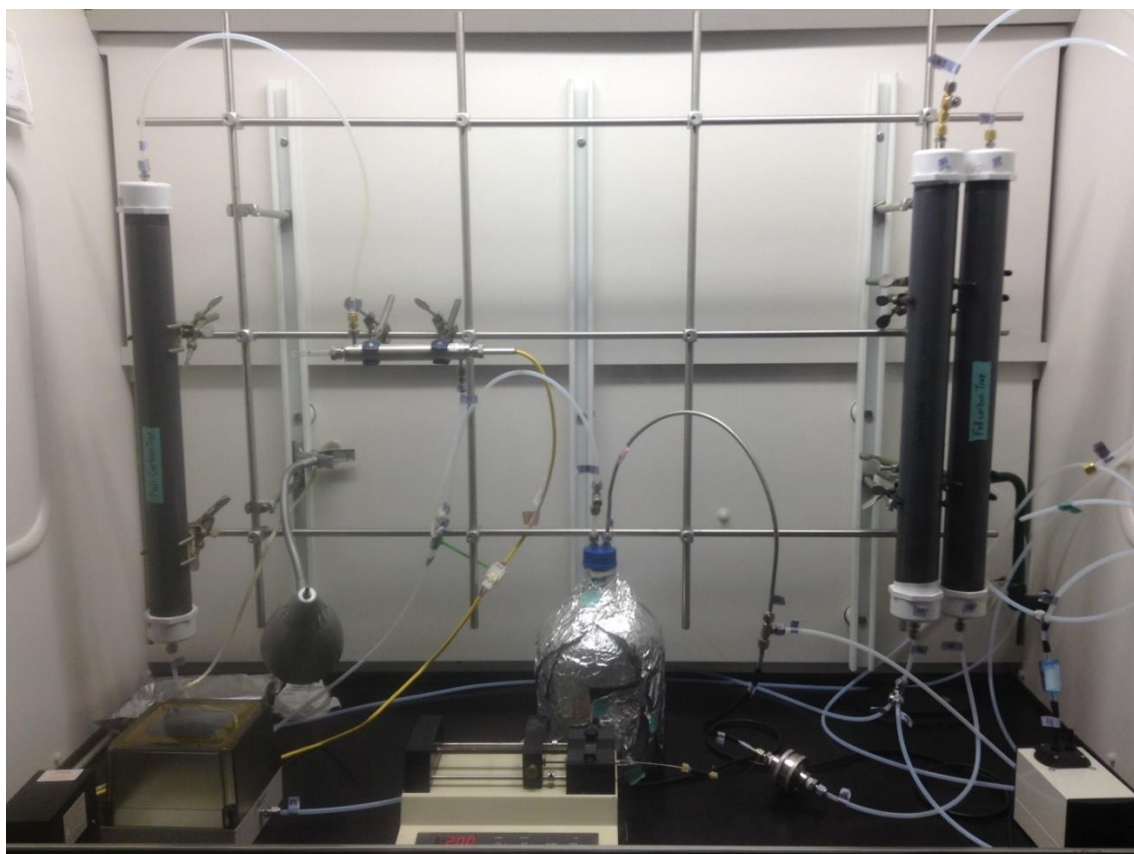


**Figure 12** Photolysis SOA generation apparatus.

Ozone (Jelight Co. Inc., Model 610; 2 – 3 ppm) flowed at a rate of ~2.5 L/min to react with  $\alpha$ -pinene (Sigma-Aldrich) vapors flowing into the gas stream through a borosilicate capillary at 20  $\mu$ L/hr. SOA was generated in a 5 L glass jar and collected on a Zefluor Teflon filter (1.0  $\mu$ m pore size, 47 mm diameter) at a rate of ~1 L/min for three hours before the filter was removed. The carbon traps assured

the air was clean, and no black carbon particles were observed on the SOA loaded filters. The mass of the filter was recorded before and after collection to determine the mass of SOA collected and aid in concentration calculations. Filters were frozen immediately after collection, before photolysis, to prevent reactions on the filter from occurring before analysis could be started.

### 3.2.2 Atmospheric Aging through Photolysis

To best mimic the atmosphere, while controlling interfering variables, photolysis was conducted in a sealable, near air-tight box (**Figure 13**), referred to as the miniaturized chamber box or simply “the box” throughout this manuscript.

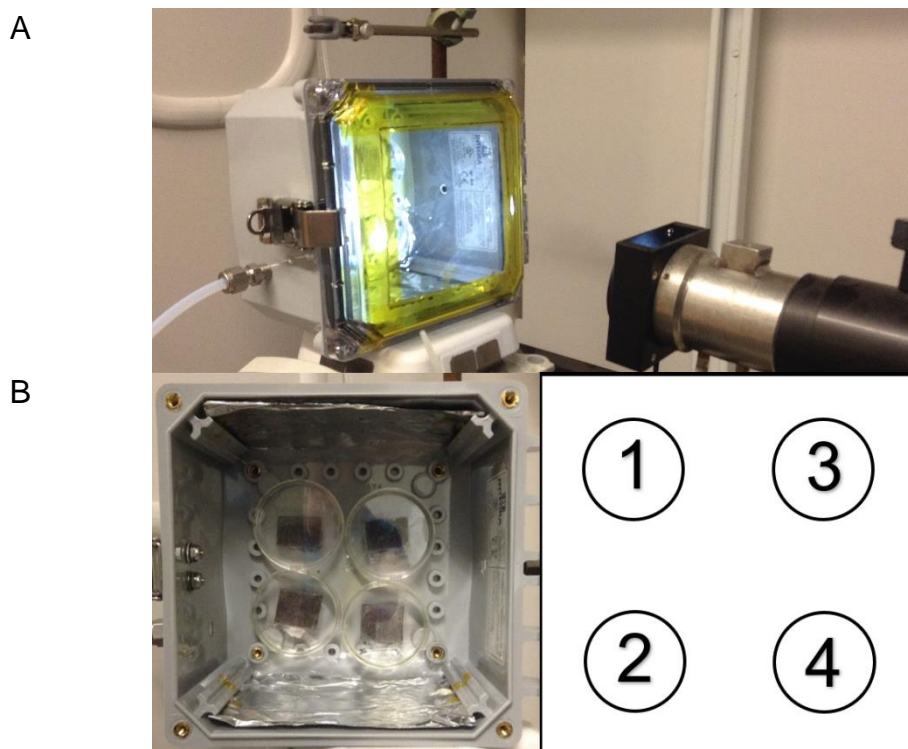


**Figure 13** (A) The box setup ~8 in. in front of the xenon arc lamp. (B) Inside the box where the filters are in Positions 1, 2, 3, and 4.

Generated zero air (EnviroNics® Series 7000), synthetic air containing less than 0.1 ppm of hydrocarbon impurities, was let into the box (1 L/min) containing four unfrozen SOA filters. A xenon arc lamp (Newport, Oriel Instruments U.S.A., lamp

power 50 – 500 W) was used to imitate sunlight as it emits radiation with similar wavelengths. To reduce interference of the incoming light, a hole was cut in the lid of the box and covered with Teflon film. Filters underwent various time exposures to the arc lamp; the details are summarized in Appendix B.

### **3.2.3 ATR-FTIR Analysis: Investigating Changes in SOA Functional Groups**

When a time exposure was complete, a filter was removed from the box and a small slice of the filter was taken for ATR-FTIR analysis. Tweezers were used to grab the filter's edge where there was visibly no SOA residue, and a slice was taken using Teflon-coated scissors.

IR was used to observe any changes in functional groups as exposure to light progressed. IR spectra was collected using a Shimadzu IRTracer-100 MIRacle 10 instrument where filter slices were placed on the diamond crystal ATR probe with the following parameters: scanning range 4000 – 400  $\text{cm}^{-1}$ ; number of scans 45; resolution 4; apodization Happ-Genzel; measurement mode %Transmittance. In ATR-FTIR, a beam of infrared light penetrates micrometers into the loaded sample before the light is reflected back and analyzed by a detector where the absorption can be measured. Molecules selectively absorb radiation at specific wavelengths causing a change in dipole moment and, therefore, the vibrational energy level goes from the ground state to an excited state. The frequency of an absorption peak is determined by this vibrational energy gap. The resulting data can give structural information on the type of functional groups in organics. Since the mixture studied in this thesis is complex, with many different molecules with different types of functional groups (as seen in

Chapter 2), the absorption peaks are broad and molecular level identification is not possible. Instead, ATR-FTIR analysis can show if shifts in the population of functional groups in the mixture occur as a result of photolysis.

### **3.2.4 UV/Vis Analysis: Investigating the Change in Efficacy of SOA**

#### **Absorption Properties**

The remaining filter, after the slice used for IR analysis, was extracted for UV/Vis analysis. The filter was cut into small pieces using Teflon-coated scissors, the slices collected in a baked, glass vial (described in detail in the next chapter) with ~2 mL ACN added. The vial was agitated to extract the SOA from the filter for ~20 minutes; then the solution was dried with ultrapure nitrogen until the ACN had completely evaporated (~30 minutes). Using 200  $\mu$ L of Milli-Q® water (MilliporeSigma), the sample was reconstituted and agitated until small, white flecks could be seen in the solution. 20  $\mu$ L was set aside in a smaller clean vial for AMS and Orbitrap MS analysis; the remaining 180  $\mu$ L was used for UV/Vis analysis.

A PerkinElmer Lambda 35 spectrometer, with deuterium (D2) and tungsten halogen lamps, collected spectra. The D2 lamp provides ultraviolet light with wavelength range from 190 – 370 nm while the tungsten lamp provides visible light with wavelength range from 320 – 1100nm. For the purposes of this thesis, a wavelength range of 200 – 550 nm was analyzed with a lamp change occurring at 326 nm, a slit width of 1.00 nm, and a scan speed of 480 nm/min. Due to the initial small volumes being analyzed, a super microcuvette (ThorLabs, UV Fused Quartz, CV10Q100, 100  $\mu$ L) was chosen.

The UV/Vis analysis provides data on the absorption constant as a function of wavelength. This allows for the observation of how SOA absorption efficacy changes over time and with exposure to light. Most previous research has focused on the absorption properties of fresh SOA that has not been aged. This research will give a more accurate prediction as to what happens to aerosols in the atmosphere as they are irradiated over multiple days.

### **3.2.5 Mass Spectrometry Analysis: Determining SOA Concentration and Molecular Weight**

A high resolution time of flight (HR-TOF) AMS (Tofwerk, AG) was used to provide the concentration of organics in the solution, along with a Thermo Electron Corporation, Finnigan LTQ XL Orbitrap, with an ESI ion source to provide the average molecular weight of SOA extracted from the filter.

A majority of the SOA loaded filters presented in this thesis have not been analyzed by the AMS and estimates have been used for their concentrations. In the future, to determine the concentration of SOA extracted, a calibration curve first needs to be constructed. Two internal standards (IS) will be used: 1) mannitol (Sigma-Aldrich) as the organic internal standard and 2) isotopically labelled ammonium nitrate ( $\text{NH}_4^{15}\text{NO}_3$ , Sigma-Aldrich) as the inorganic internal standard. The calibration curve will be created by plotting organic/IS measurements as a function of  $[\text{organic}]/[\text{IS}]$ . Once this is done, SOA samples can be measured and their concentrations determined.<sup>6</sup>

A preliminary method for the determination of molecular weight is presented here. 100  $\mu\text{L}$  of Milli-Q was mixed with 3  $\mu\text{L}$  of SOA extraction and

electrosprayed into the Orbitrap, with voltages between 4.0 – 4.4 kV, at a flow rate of ~2  $\mu\text{L}/\text{min}$ . Four collections were taken per sample:

<b>Resolution</b>	<b>Run Time</b>	<b><i>m/z</i></b>
60,000	~7 min	120 – 1000
100,000	~12 min	120 – 1000
100,000	~7 min	250 – 1000
30,000	~7 min	120 – 1000

The *m/z* range was changed for the third collection because the signal of the peaks  $>250$  *m/z* was being overwhelmed by the signal of the peaks  $<250$  *m/z*. By cutting out the lower *m/z*, it allows the peaks  $>250$  *m/z* to dominate the signal scale for better observation.

### 3.3 Data Analysis and Discussion

#### 3.3.1 Calculating Epsilon through Calibration Curves

Absorption cross sections,  $\sigma$ , specify a molecule's absorption properties, or its absorption efficiency, by measuring the effective area of the molecule that a photon needs to traverse in order to be absorbed. An absorption cross section corresponds to the molar absorption coefficient,  $\epsilon$ , via the following equation:

$$\sigma(\text{cm}^2) = \frac{2.303(\text{cm}^3\text{L}^{-1})}{6.02 * 10^{23}(\text{mol}^{-1})} \epsilon(\text{Lmol}^{-1}\text{cm}^{-1}) \quad (1)$$

The relationship between the absorption cross section and the molar absorption coefficient can be seen through the following derivation.<sup>78</sup>

$$T = \frac{I}{I_0} \quad (2)$$

where T is the transmittance, I is the intensity of outgoing light after it's passed through the sample, and  $I_0$  is the incident intensity, or the intensity of incoming light. Absorbance is defined by

$$A = -\log \frac{I}{I_0} \quad (3.1)$$

therefore  $A = -\log(T)$  (3.2)

therefore  $T = 10^{-A}$  (3.3)

From the Beer-Lambert Law,

$$A = \epsilon lc \quad (4)$$

where  $l$  is the length of the sample that light passes through and  $c$  is the molar concentration. Using equations 3.3 and 4, as well as  $c$  defined as  $\frac{n}{N_A}$ , where  $n$  is the density of absorption centers within the molecule and  $N_A$  is Avogadro's number, equation 5 is derived.

$$10^{-A} = 10^{-\epsilon lc} = 10^{-\epsilon l n / N_A} \quad (5)$$

Additionally, from the Beer-Lambert Law, to bring in the cross section variable, is the following equation:

$$I = I_0 e^{-n\sigma l} \quad (6.1)$$

therefore  $\frac{I}{I_0} = e^{-n\sigma l} = T$  (6.2)

Based on equation 6.1, combined with equation 5,

$$e^{-n\sigma l} = 10^{-\epsilon l n / N_A}$$

Taking the natural log of both sides,

$$-n\sigma l = \ln(10) \left[ -\epsilon l \left( \frac{n}{N_A} \right) \right]$$

$$\sigma N_A = 2.303\epsilon$$

$$\epsilon = \frac{\sigma N_A}{2.303}$$

Therefore, the absorption cross section can be determined from UV/Vis measurements through

$$A = \frac{\sigma ln}{2.303} \qquad \sigma = \frac{2.303A}{lcN_A}$$

The molar absorption coefficient was calculated by creating a calibration curve of absorption as a function of concentration for a single wavelength. To make a calibration curve from the UV/Vis data sets, the AMS concentration (in g/L) was calculated for each dilution. For the work here, an estimate based on initial AMS data was used. Finalized concentrations will move the absorption measurements up or down the y-axis and, hopefully, will make them overlay at lower wavelengths (~245 – 250 nm). With the known mass from Orbitrap MS measurements, the molar concentration was calculated for each dilution, and from this, the number of molecules per milliliter. Calculations for Box 1.1 (meaning a filter under the conditions of Box 1 in Position 1), as an example, can be seen in Appendix B; calculations for Box 1.1 are representative of calculations and data processing for all other boxes as they are replicates, outlined in Appendix B.

Absorbance values were processed as follows. Each sample was run in the UV/Vis three times resulting in three absorbances per wavelength to account for any possible lamp flux; the average absorbance was calculated and will now be referred to as simply absorbance. Because of the lamp change at 326 nm, a step is generated in the data (**Figure 14 A**). To smooth the data, the difference in the absorbance between 326 nm and 327 nm was calculated and added to the absorbances for wavelengths 200 – 326 nm (**Figure 14 B**).



**Figure 14** Box 1.1, 24hr light, (A) showing a step in the data at 326 nm due to a lamp change and (B) smoothed. Selected total sample volumes shown for clarity.

Any absorbance above 1.5 was ignored as these values are unreliable due to too high a concentration to be accurately measured.

Once the concentrations and absorbances were processed and plotted, a line was fit to each calibration curve, the slope of which is the value of the molar absorption coefficient (**Figure 15**).

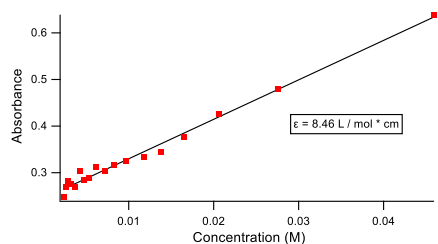


**Figure 15** Calibration curve at 310 nm for Box 1.1, 24hr light.

### 3.3.2 Calculating and Analyzing the Cross Sections

Calculating the cross sections required absorbances to be multiplied by 2.303, the natural log of 10, as described in the equations above. Cross sections were determined just as the molar absorption coefficient was; absorbance was plotted as a function of concentration for each wavelength, and the slope of the best fit line was the cross section.

Position 4 is likely being exposed to less light, or more indirect light, than the other positions in the box. This can be seen in **Figure 16**.

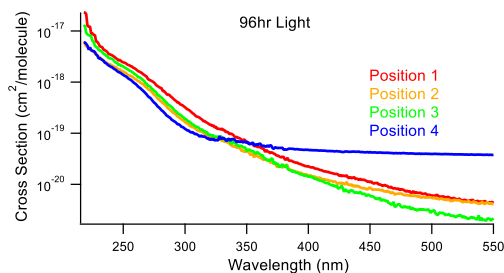


**Figure 16** Box 4, 96hr light, all positions. Position 4 is an outlier compared to the other positions.

Box 4 had filters in all positions exposed to 96 hours of light. Looking at the cross sections it is quite obvious that Position 4's absorption plateaus just before 350 nm while the other positions continue to see absorption decay at higher wavelengths. The reason for this behavior is unclear; it was not observed in other measurements. There also appears to be a slightly lower signal around 280 nm for Position 4 possibly indicating it is experiencing fewer photons from the lamp.

For this reason, Box 1's Position 4 will be replaced by Box 4.2, a position known to have the expected light exposure.

A comparison of all relevant experiments' Position 4 are shown in **Figure 17** where the shape of Box 1.4 and Box 2.4's cross sections are very similar to that of Box 4.1, 2, and 3. This indicates that the plateau of Box 4.4 is an anomaly and that, perhaps, some interference occurred during the Box 4 experiment, specifically at Position 4.

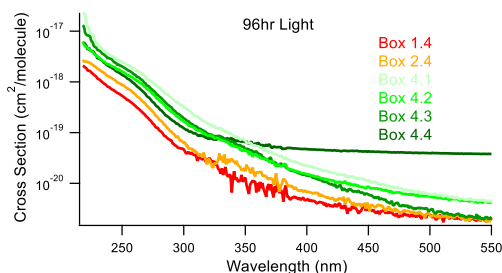


**Figure 17** Box 4 (green), 96hr light, positions compared to Box 1.4 (red) and Box 2.4 (orange), 96hr light, positions. The shape of Box 4.1, 2, and 3 are very similar to the shape of Box 1.4 and Box 2.4 thus indicating possible interference with Box 4.4 during the experiment.

Further research will involve repeating the 96 hour time exposure experiment at all four positions, focusing on the results of Position 4. Actinometry experiments will also be performed to assess the validity of Position 4.

Actinometry measures the intensity of radiation typically by determining the number of photons from a beam absorbed into a chemical reactor based on the speed of a photochemical reaction.<sup>79</sup> The following equation is used to determine radiation intensity, or photon flux.

$$J = \sum \sigma_{\lambda} \Phi_{\lambda} F_{\lambda} \Delta\lambda$$

where J is the reaction rate constant,  $\sigma$  is the cross section,  $\Phi$  is the quantum yield, and F is what is being solved for, the photon flux, all as a function of the change in wavelength.<sup>79</sup> By doing this, the radiation intensity for each position in the box will be determined in order to assess the equivalency of those positions.

**Figure 18** compares Box 1 (1 – 4 days of irradiation) to an SOA loaded filter not exposed to light nor the conditions of the box; this is considered T0.



**Figure 18** (A) Box 1 compared to an SOA loaded filter not exposed to light, T0 (dashed line). (B) Zoomed to 220 – 330 nm. Note the presence of a peak at ~280 nm for T0 that decreases for Box 1 as photolysis increases.

The dashed line of T0 has a prominent hump of absorption at ~280 nm from a large population of carbonyls.<sup>80</sup> The presence of this absorption begins to wane as photolysis increases. This likely corresponds to the loss of carbonyls and removal of chromophores from the system consistent with photobleaching.

This conclusion was explored more fully by comparing Box 1 to Box 3 (Figure 19). Box 3 consisted of filters not exposed to light but analyzed at the same time points as Box 1.

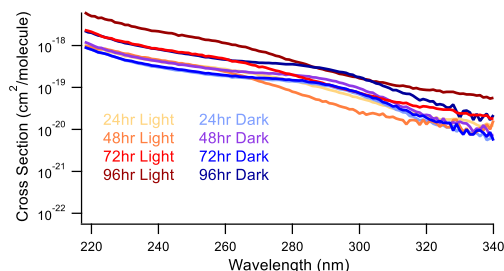


**Figure 19** Comparing Box 1 (light) and Box 3 (dark) exposures where a carbonyl absorbance peak is absent for photolyzed filters but present for non-photolyzed filters.

The 24 (Position 1), 48 (Position 2), 72 (Position 3), and 96 (Position 4) hour dark exposures all have an absorption between ~280 – 300 nm whereas the corresponding light exposures appear flatter, losing that carbonyl absorption due to photolysis. This decrease is consistent with literature results from aqueous photolysis reactions.

Due to cancellation of production of Zefluor filters, a switch to EZFlow® (Foxy Life Sciences, PTFE Membrane, 0.22 µm pore size, 47 mm diameter) filters was made. These new filters (NF) have about 1/5 the pore size of the old filters (OF). **Figure 20** shows the difference in absorption between the Zefluor and EZFlow filters.

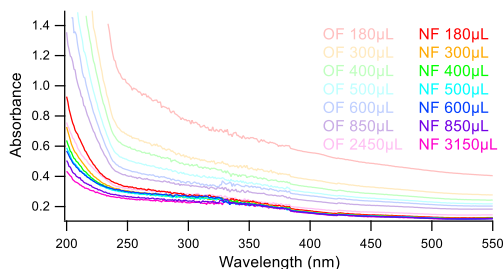


**Figure 20** Zefluor (OF) absorbance compared to EZFlow (NF) absorbance, both blank, non-SOA loaded filters. OF, in general, has a higher absorbance than NF across the range of wavelengths. Selected total sample volumes shown for clarity.

It's worth noting the lower absorption the EZFlow filters have, in general, compared the Zefluor filters. While the absorption contribution of the filters themselves should never interfere with the absorption results from SOA samples (because SOA is being extracted from the filter), should any contamination be occurring, EZFlow filters would provide less of an interference. From this alone, one might consider these filters to be a better choice. However, it is possible the very small pore size is hindering the SOA loading process as seen by the following.

EZFlow filters were used in Box 5 and Box 6 experiments. While the absorbances from Box 1.4 (96hr light) can't directly be compared to the absorbances of Box 6.1 (120hr light), due to different photolysis times, it is worth noting the very low absorbances of SOA from the EZFlow filter compared to the Zefluor filter (**Figure 21**).

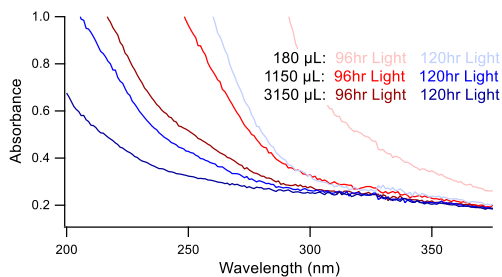


**Figure 21** Box 1.4, 96hr light, compared to Box 6.1, 120hr light. Note the low absorbances associated with Box 6 using the EZFlow filter. Selected total sample volumes shown for clarity.

Box 1's absorbances are well exceeding 1.0, even before the wavelength range limit of 200 nm, at its highest total sample volume, while Box 6's absorbances quickly fall to about half of that at the same dilution. In addition, as seen in the table of samples in Appendix B, Zefluor filters have an average SOA mass loading of 2.87 mg while EZFlow filters have an average SOA mass loading of 0.85 mg — granted only two filter masses are available at this time. Again, many more future experiments are needed to explore what changing to these EZFlow filters is doing in terms of SOA mass loading.

Some SOA is being loaded onto the EZFlow filters, however. **Figure 22** shows Box 5, a box of non-loaded, blank filters, compared to SOA loaded filters of Box 6.



**Figure 22** Box 5 (dark) compared to Box 6 (light), (A) Position 1 at 120hr time exposure and (B) Position 2 at 144hr time exposure. The higher absorbances of Box 6 indicate EZFlow filters are collecting some SOA during loading. Selected total sample volumes shown for clarity.

Because Box 6 is showing absorbances greater than that of Box 5, SOA must be present in some capacity on EZFlow filters. **Figure 23** shows Box 6's longer photolysis times of 120 and 144 hours.

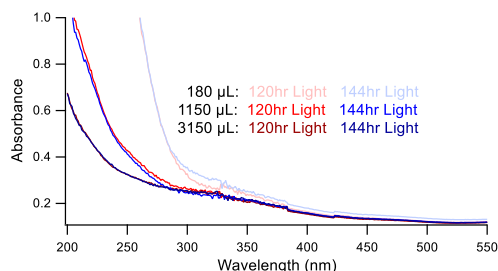


**Figure 23** Box 6.1, 120hr light, and Box 6.2, 144hr light.

Not much difference can be seen between absorbances of the five and six day exposures. Perhaps SOA's rate of reactivity begins to plateau at this point. Cross section analysis of these longer photolysis times will be investigated.

Future research will continue to explore the result of photolysis on the carbonyl absorption peak as well as continue to perfect the methodology of this

experiment. Replicates will be done for both light and dark exposures, and an increased number of time points will be added; the validity of Position 4 will be explored through actinometry; UHR-MS average molecular weight and molecular composition information will be collected for Boxes 2 – 6 as well as blank and T0 samples.

### **3.3.3 ATR-FTIR Analysis**

Just as the variance in SOA mass loadings for each filter effects the UV/Vis analysis results, so does the variance in SOA loading thickness for each filter effect IR analysis. Film thickness is something that can't and isn't attempted to be controlled by this lab at this point. Therefore, no quantitative functional group changes can be drawn from the IR data presented here. IR analysis is simply showing the shape change of absorption peaks as a result of increased photolysis, supporting the results from UV/Vis analysis that the SOA sample is changing.

**Figure 24** shows the percent transmittance, normalized to the Teflon peak, of Box 1. Peaks of importance are that of the OH, CH, and carbonyl stretching. A table summarizing the range and type of stretching can be found in Appendix B.

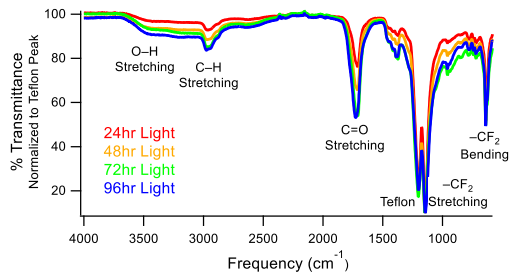


**Figure 24** IR of Box 1 Position 1 (red), Position 2 (orange), Position 3 (green), and Position 4 (blue). Transmittance normalized to the Teflon peak.

IR data sets were converted from percent transmittance to absorbance using  $A = 2 - \log T$  and then normalized to the maximum absorbance value for each time exposure; this was the Teflon peak. To test methodology, an IR comparison was made between a blank filter, a morning SOA loaded filter, and an afternoon SOA loaded filter. As shown in **Figure 25**, these filters can be considered equal and do not seem to be affected by the initial set up of the apparatus at the beginning of the day.

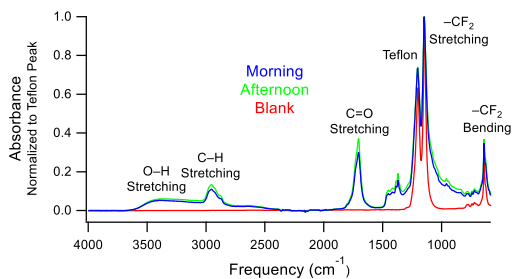


**Figure 25** A comparison of morning (blue, 110218a) and afternoon (green, 110118p) SOA loaded, Zefluor filters. The similarity in absorbance indicates morning and afternoon loaded filters can be considered equal. The blank (red) is 012919 filter.

The UV/Vis data analysis shows an important point of investigation seems to be the carbonyl peak at  $\sim 1700 - 1750 \text{ cm}^{-1}$ ; thus, IR peak shape analysis focused on that range. Using the Igor Pro 7 software package, a series of parabolas were fit to the raw data peak to find the area under that peak. For example, **Figure 26** A shows the absorbance of Box 1.1 zoomed to the carbonyl peak, and Figure 26 B shows the peak fitting.



**Figure 26** (A) Box 1.1, 24hr light, carbonyl absorbance peak. (B) Fitted peak picking of Box 1.1.

In Figure 26 B, the top of the figure shows how well the estimated peaks fit the raw data peak, the residual calculation; a straight line at zero would be ideal and

indicate a perfect fit. The middle of the figure shows the sum of the fitted peaks (in blue) overlaid on the raw data peak (in red). Last in the figure shows the shape of the four peaks used in fitting. The shape changes of these four peaks, as well as the change in the area under the raw data peak will be analyzed.

Four peaks were chosen to be fit to the raw data: Peak 0 at  $1641.5\text{ cm}^{-1}$  with a width of  $40\text{ cm}^{-1}$ , Peak 1 at  $1708\text{ cm}^{-1}$  with a width of  $30\text{ cm}^{-1}$ , Peak 2 at  $1735.1\text{ cm}^{-1}$  with a width of  $30\text{ cm}^{-1}$ , and Peak 3 at  $1770.3\text{ cm}^{-1}$  with a width of  $40\text{ cm}^{-1}$ . These constraints were used for every sample analyzed. The height of the peaks varied based on the fitting parameters of the program. These peaks do not have any correlation to the functional groups; they are simply the minimum number of peaks needed to initially fit the peak from Box 1.1. This analysis provides a more numerical view of the shape changes observed in the carbonyl peak as a function of irradiation.

Box 1 of photolyzed filters was compared to Box 3 of non-photolyzed filters and a filter of T0 (filter 110118p) in **Figure 27** A and B. Peak fitting comparisons of Box 1.1, Box 1.4, Box 3.1, Box 3.4, and T0 will be presented here. All other peak fitting data can be found in Appendix B.

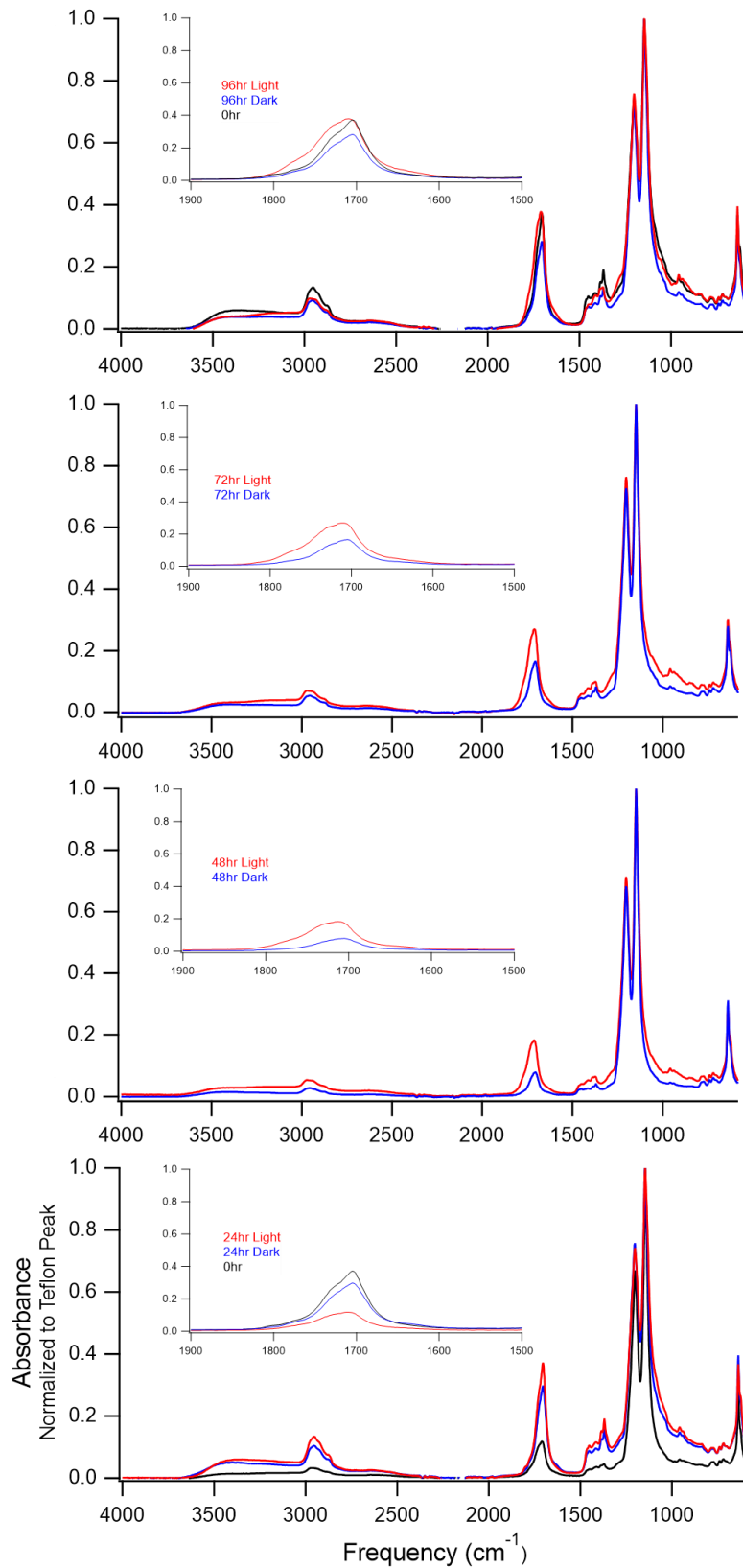


**Figure 27 A** Box 1 (light, red) and Box 3 (dark, blue) IR comparison at all positions. 0hr (black) is SOA loaded 110118p filter never exposed to any box conditions.

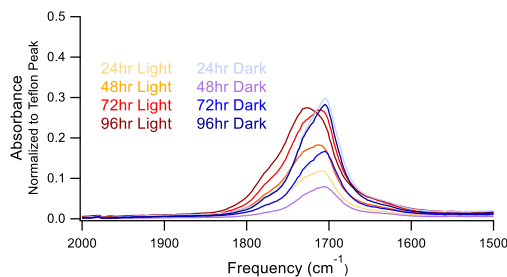


**Figure 27 B** Compiled Box 1 (light) and Box 3 (dark) carbonyl peaks at all positions.

In Figure 27 B, the carbonyl absorbance peak for the dark filters (Box 3, purple and blue spectra) seems to be slightly red-shifted compared to the photolyzed filters (Box 1, yellow and red spectra). Future investigation might explore the relationship between this observed IR red shift and the red shift discussed in Chapter 2 regarding a carbonyl in a ketone rather than an aldehyde functional group. This shift may also be influenced by the changes of carbonyls to other C=O functional groups like acids and esters. It is not expected that there are many, or any, C=C functional groups in the SOA. Ozone is a good oxidant and is expected to have reacted with any unsaturated carbons in the gas phase and on the filter.

In **Figure 28**, a shape change can be seen in Peaks 0, 2, and 3 in the span of a day of photolysis. The comparison of the photolyzed box and the dark box (**Figure 29**) show there is a shape difference between Peaks 2 and 3. **Table 1** summarizes the area of each fitted peak as well as the percentage of the total area that peak accounts for.



**Figure 28** (A) 0hr filter compared to (B) Box 1.1, 24hr light, peak fitting. Note the change in shape of fitted Peaks 0, 2, and 3. The y-axis is absorbance normalized to the Teflon peak.

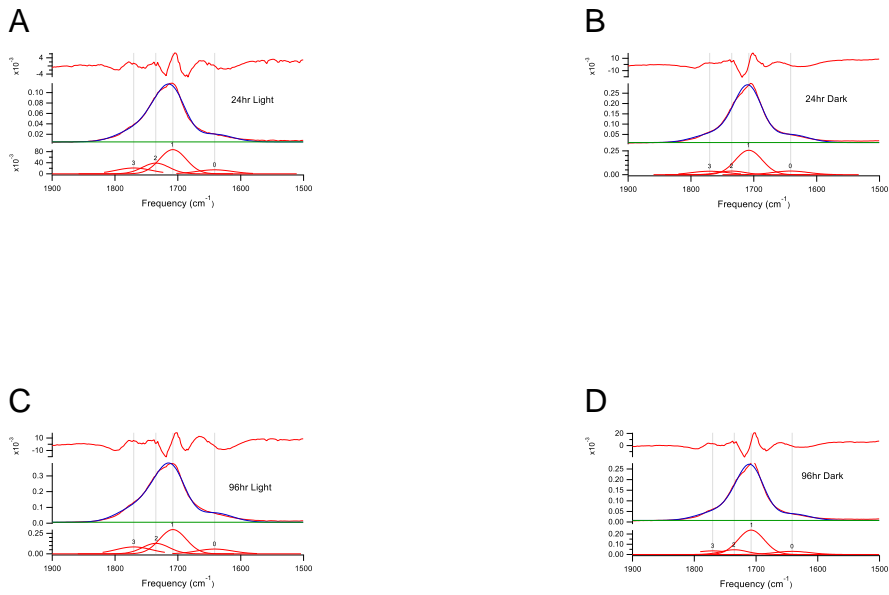


**Figure 29** Peak fitting of (A) Box 1.1, 24hr light, (B) Box 3.1, 24hr dark, (C) Box 1.4, 96hr light, and (D) Box 3.4, 96hr dark. A shape change can be seen in fitted Peaks 2 and 3 between Box 1 and Box 3. The y-axis is absorbance normalized to the Teflon peak.

**Table 1 Summary of Fitted Peak Areas**

<b>0hr</b>	<b>Frequency (cm<sup>-1</sup>)</b>	<b>Area</b>	<b>Area Sum</b>	<b>% of Area</b>
Peak 0	1641.5	2.2476	25.0239	9.0
Peak 1	1708	16.876		67.4
Peak 2	1735.1	2.6009		10.4
Peak 3	1770.3	3.2994		13.2
<b>24hr Light</b>				
Peak 0	1641.5	1.0241	9.2171	11.1
Peak 1	1708	4.6462		50.4
Peak 2	1735.1	2.0544		22.3
Peak 3	1770.3	1.4924		16.2
<b>24hr Dark</b>				
Peak 0	1641.5	2.7023	20.9406	12.9
Peak 1	1708	13.645		65.2
Peak 2	1735.1	2.0178		9.6
Peak 3	1770.3	2.5755		12.3
<b>96hr Light</b>				
Peak 0	1641.5	4.112	32.5629	12.6
Peak 1	1708	15.714		48.3
Peak 2	1735.1	6.7714		20.8
Peak 3	1770.3	5.9655		18.3
<b>96hr Dark</b>				
Peak 0	1641.5	2.1627	19.7689	10.9
Peak 1	1708	12.663		64.1
Peak 2	1735.1	2.4472		12.4
Peak 3	1770.3	2.496		12.6

The peak percentages are relatively stable for both photolyzed and non-photolyzed peaks across all time exposures. A main shape shift can be seen between Peaks 1 and 2 (1708 and 1735.1 cm<sup>-1</sup>). Photolyzed filters have a lower percentage for Peak 1 than that of the dark filters, yet a higher percentage for Peak 2.

Box 6 could not be fit for peak picking. **Figure 30 B** particularly shows the difficulty presented when trying to fit these two peaks and **Figure 30 A** shows there may not be a significant enough peak at ~1700 cm<sup>-1</sup> anyway.



**Figure 30** (A) IR of Box 6.1, 120hr light, (red) and Box 6.2, 144hr light (blue). (B) IR of Box 6 zoomed to the carbonyl absorbance peak.

Once again, the different characteristics between the two filters used in this experiment, and their possible influence on the data, needs to be better understood. Just as the Zefluor filter differed from the EZFlow filter for the UV/Vis analysis, so do the filters differ in IR analysis (**Figure 31**).

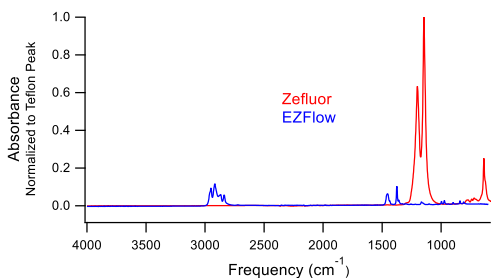


**Figure 31** Zefluor (red) and EZFlow (blue) IR, normalized to the Teflon peak.

Part of the OH stretching in the collected IR data sets is likely from water. Virginia is very humid, and the water in the atmosphere interferes with IR readings. Future experiments might consider setting up a box over the ATR crystal to ensure exact relative humidity measurements. Additionally, controlling film thickness as SOA is being loaded onto the filters should be explored.

## Chapter 4: Organic Deposition through Dew Analysis

### 4.1 Motivation for Investigating Organic Deposition

Aerosols should not only be of concern when they exist in the atmosphere, but also should be considered for their impacts once they have been removed. Particles are removed from the atmosphere through deposition which is dictated by particulate mechanisms — impaction, sedimentation, and diffusion.<sup>10</sup> Reactive organic carbons (ROCs) in the atmosphere exist in the gas phase as volatile organic compounds (VOCs) as well as the condensed phase as aerosols or cloud droplets. Knowing the fraction of emitted ROCs that are oxidized to completion as CO and CO<sub>2</sub> as opposed to those lost to surfaces via deposition is an area of active research. Current models deal with deposited ROCs onto Earth's surfaces by removing them entirely from the modeled atmosphere. Yet, in the lab, deposited organic molecules can react by heterogeneous oxidation as well as photolysis to produce small VOCs, proving that current atmospheric box models do not capture the return of deposited carbon back into the atmosphere.<sup>8,21,23,39,40</sup> Quantifying and characterizing the extent of deposition and the effects of subsequent reactions will improve current atmospheric models and their predictions.

Dew forms on nights when there is little-to-no cloud cover or wind, and it forms when the air is humid. For dew to manifest, surfaces must radiate their heat until their temperature has become equal to or lower than a critical temperature called the dew point. When this happens, water vapor contacting a cold surface condenses at a rate greater than that of evaporation.<sup>81,82</sup> After the dew begins to form, organic compounds from the atmosphere are deposited

throughout the night. Additionally, dew is forming on surfaces which often have had dry deposition of material occurring throughout the previous day(s).

Previous research has focused on inorganic ions and small acids found within dew droplets, but little is known about the organic composition or how this can vary by location, season, and possible chemistry occurring while the dew evaporates in the morning. Many deposited, small organic compounds are water soluble and can potentially re-volatilize off a surface as water evaporates. The identities of those organic compounds, and the magnitude in which they re-enter the atmosphere, are still unknown. Environmental surface waters, including dew, provide a good system to begin investigating these processes. Grass blades provide a suitable outdoor surface to investigate aerosol deposition and chemical composition to identify and quantify small organics.

Researching the changes in composition of organic aerosols of polluted regions reveals information on both aerosol distribution and whether particles are created from natural or anthropogenic sources. Specifically, this research on organic carbon deposition lays the groundwork for an experimental platform to inform future studies on atmospheric organics to improve understanding of chemical transport and air quality, as well as to provide data on organic composition, potential clues about localization or seasonal changes, and whether re-emission into the atmosphere is occurring during dew evaporation.

## 4.2 Experimental Methods

### 4.2.1 Materials and Collection Method

To avoid contamination of the organics being collected and analyzed, it was essential that any residual organic material on the collection apparatuses and in the collection vials was removed. To achieve this, all glassware was first placed in an oven and baked at 450°C for six hours to burn off any organics.

Dew collection occurred during the early morning. A glass rod was swiped over an area of wet blades of grass then tilted vertically to allow the droplets of dew to drip from the rod and into a baked, glass vial. This was done until about 8 – 10 mL was collected. After some experimentation, the glass rod was later replaced with a stainless steel, Fisherbrand™ Scoopula® spatula which was able to collect more dew droplets in its trough-like shape with one swipe across the grass blades. This dew solution was then pushed through a polytetrafluoroethylene (PTFE) or Teflon filter (Thermo Fisher Titan3, 0.2 μm) to remove grass, dirt, bacteria that would destroy the organic compounds, and any other foreign particles. This fluoropolymer is hydrophobic and nonreactive due to the high electronegativity of fluorine and the strength of the bonds between carbon and fluorine. The sample was then placed in a freezer until needed, at which time it was thawed for analysis.

Initial tests on dew water samples in syringe fed ESI set ups clogged the spray capillary. It was determined that sample preparations required the dew solutions to undergo solid phase extraction (SPE)<sup>83,84</sup> A nonpolar Bond Elut™

PPL syringe (Agilent Technologies, 500 mg, 6 mL, **Figure 32**) with a styrene-divinylbenzene (SDVB) polymer cartridge was used.

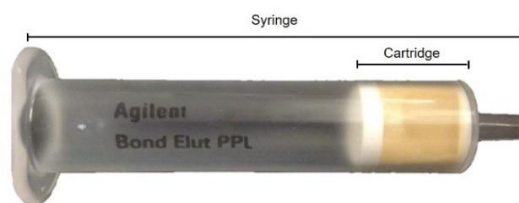


**Figure 32** Agilent Technologies PPL syringe.

The syringe was chosen for its ability to retain polar analytes, its large, hydrophobic surface area, and its large pore size allowing for easy flow of particulate rich water samples. It was first rinsed with two cartridges (~4.4 mL) of MeOH<sup>29</sup> to prepare the syringe, ensuring the sample would immediately be absorbed into the cartridge. A Pasteur pipet was used to load the dew sample into the PPL syringe to be filtered, collecting the eluate of elements of the dew sample that did not stick to the cartridge. Next, at least two cartridges of Milli-Q water spiked with one drop of 36 – 37% HCl was used to wash the PPL syringe; this was also collected. The PPL syringe was then dried by placing it under pure nitrogen flow for about 5 – 10 minutes. After the syringe cartridge was dry, a final collection was taken by washing with at least one cartridge of MeOH. This last eluate collection was analyzed via mass spectrometry. Preparing the PPL syringe for reuse required MeOH wash of at least 25 mL.

#### **4.2.2 Preliminary Results**

Initial sample analysis was done on a mass spectrometer (Thermo Finnigan LCQ Deca) linear ion trap which used a 2 mL blank of Milli-Q water spiked with 2  $\mu$ L of formic acid for background, followed by a dew sample also

spiked with 2  $\mu\text{L}$  of formic acid. This initial sample was too dilute to see any peaks and remaining samples needed to be concentrated.

Since water takes a long time to evaporate under gentle  $\text{N}_2$  flow, lyophilization, the process of freeze drying a sample in a vacuum, was chosen as the method of concentration. During lyophilization, volatile material in the sample is lost. AMS offline mass spectra for fresh dew and lyophilized dew samples (**Figure 33**) was taken to ensure this method would leave enough dew sample later for analysis.

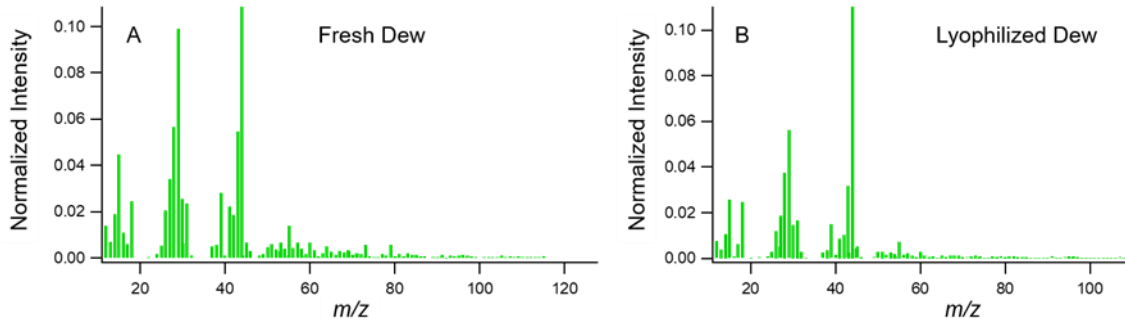


**Figure 33** AMS offline mass spectra for (A) fresh dew and (B) lyophilized dew. The change between the two samples is consistent with the loss of more volatile organics during lyophilization.

The difference between the two spectra is consistent with the loss of more volatile compounds during lyophilization; however, sufficient mass remained for analysis. Thus, this is a valid method for concentrating dew samples.

The lyophilized sample was run again on the linear ion trap (**Figure 34**). The sample concentration seemed to be remedied, but, eventually, the sample clogged the capillary. To clean the dew samples, SPE procedures were initiated using the PPL syringe as described in the Materials and Collection Method section. SPE is a commonly used method to prepare dissolved organic matter samples from other sources, such as lakes, oceans, etc.

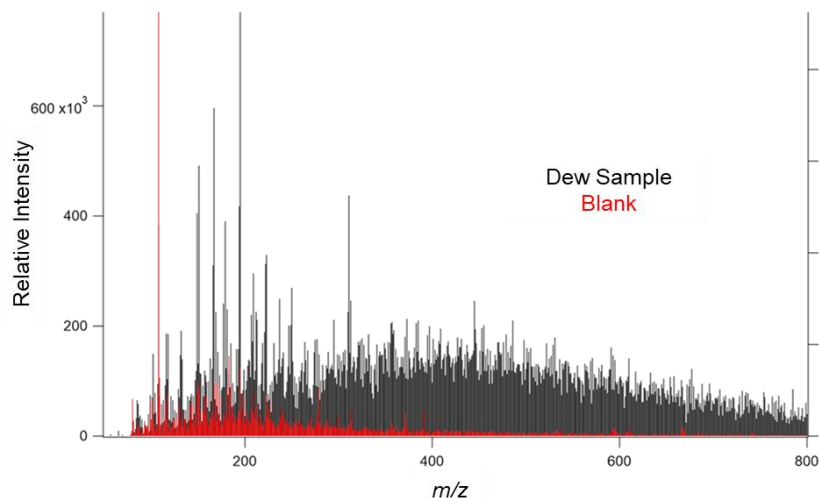


**Figure 34** Mass spectrum of a dew sample (black) and Milli-Q water (red).

At this point, the samples were ready for the next round of data collection. A high resolution, Fourier transform ion cyclotron resonance mass spectrometer (FTICR-MS), located at Old Dominion University, was used to generate mass spectra for the dew sample. This analysis revealed a complex organic mixture along with large sugars (**Figure 35**). Sugars are likely from guttation: a process where material is expelled from plants at night.<sup>85</sup>

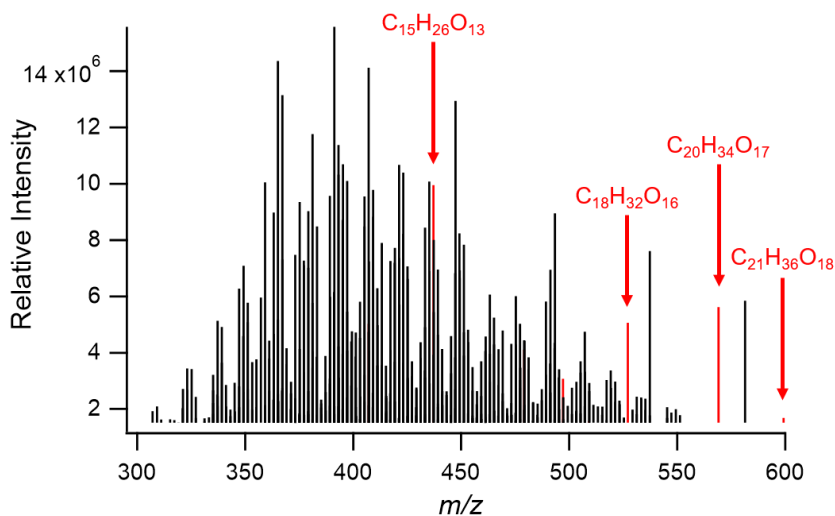


**Figure 35** Mass spectrum of a solid phase extracted dew sample analyzed by an FTICR at Old Dominion University. A complex mixture of organic molecules was observed along with large sugars (red).

### 4.2.3 Future Research

Dew samples will continue to be lyophilized to increase concentration for future analysis. This method of freeze drying the samples will be done by placing them under a vacuum, preventing the samples from being contaminated by organics and increasing the concentration through the loss of water; however, some volatile compounds will be lost as well.

SPE is a good preparation technique for soft ionization analysis, yet the material that is extracted may or may not be reproducible. Therefore, the reason initial tests clogged the capillary will be investigated.

To probe the chemical identities of the components, samples will be derivatized with N,O-Bis(trimethylsilyl)trifluoroacetamide (BSTFA) and solvent extractions will be performed. This will enable composition identification done through gas chromatography mass spectrometry (GC/MS) using retention times from the GC and electron ionization fragmentation/fingerprint matching from the MS. After the most abundant compounds have been identified, standards will be used to calibrate the GC/MS to quantify these compounds across different samples. This process will be imposed on two different types of dew samples: “clean” samples that have been collected from Teflon sheets and natural dew water that has been collected from grass and leaves using glass rods or Scoopulas.

Natural dew complexity can vary from surface to surface and is based on each surface’s history. To characterize this complexity, direct injection into an UHR-MS (either an Orbitrap or FTICR) via soft ionization (likely ESI) will be done.

This will provide the elemental formulas for a majority of the organic materials with sub-ppm mass accuracy in a single measurement.<sup>86</sup>

Future research will continue to focus on characterizing chemical composition and changes throughout aging processes on both natural and cleaned surfaces by looking at impermeable surfaces, like urban buildings including tiles, walls, windows, etc.; biologic surfaces, like leaves and grass; and aqueous films and droplets, like dew. Laboratory experiments will probe deposited ROC by evaluating reactive uptake of oxidized VOCs into a sample and observing the chemical reactions that occur as samples are cycled in relative humidity, irradiated, and exposed to oxidants. Organic material remaining on the surface after these aging reactions will be characterized using advanced MS techniques and fluxes will be integrated into existing atmospheric models to better constrain organic carbon cycling in the atmosphere.

## Chapter 5: Conclusion

Combining the strengths of IR action spectroscopy, mass spectrometry, and computational modeling proved to be a successful analytical technique in generating detailed structural information of isolated ion populations. While this thesis demonstrated an acceptable spectral match of a cis-Pinonic Acid standard to an unknown, it is understood that this technique does not necessarily positively identify the structures of unknowns; however, implementing this method provides considerable support for assignments of isomers. Even if exact structures of unknowns cannot be determined, this system will significantly reduce the number of possible candidates.

To move away from research of photochemical reactions in water droplets and increase the research of ambient organics in the gas phase, we are building an experimental foundation by developing methods for a more thorough analysis of photolysis of complex SOA films. From the ATR-FTIR results, we know the SOA film is changing with increased exposure to light. The UV/Vis analysis of photolyzed SOA cross sections showed a decrease in absorption for carbonyls (~280 nm), indicating chromophore bleaching. The red-shifted carbonyl absorbance peak from the comparison of photolyzed and non-photolyzed filters may denote shifts in C=O components in SOA. These likely include unknown amounts of ketones and aldehydes as well as carboxylic acids and esters.

The next steps in this project will focus on collection of concentration data; evaluation of the efficacy of the new, EZFlow filters; replicates of the box experiments, especially looking at Position 4; continued comparison of

photolyzed and non-photolyzed exposures; increased time exposures; and further investigation of the changes in absorption of the carbonyl peak. This research will give insights to improve atmospheric models by providing more accurate data of aged SOA, replacing the current inputs of molecular composition and absorption cross section data from fresh SOA.

The O'Brien lab will continue to research condensed phase organic carbon (both aerosol and deposited films) to explore changes in composition of organic aerosols in different regions, gaining insight into aerosol chemical distributions and aerosol sources.

Preliminary dew analysis resulted in the realization that dew sample concentration needs to be increased, and samples need to be cleaned more thoroughly. Investigation into why these samples clog the capillaries will be conducted, and lyophilization as a concentration method will be continued.

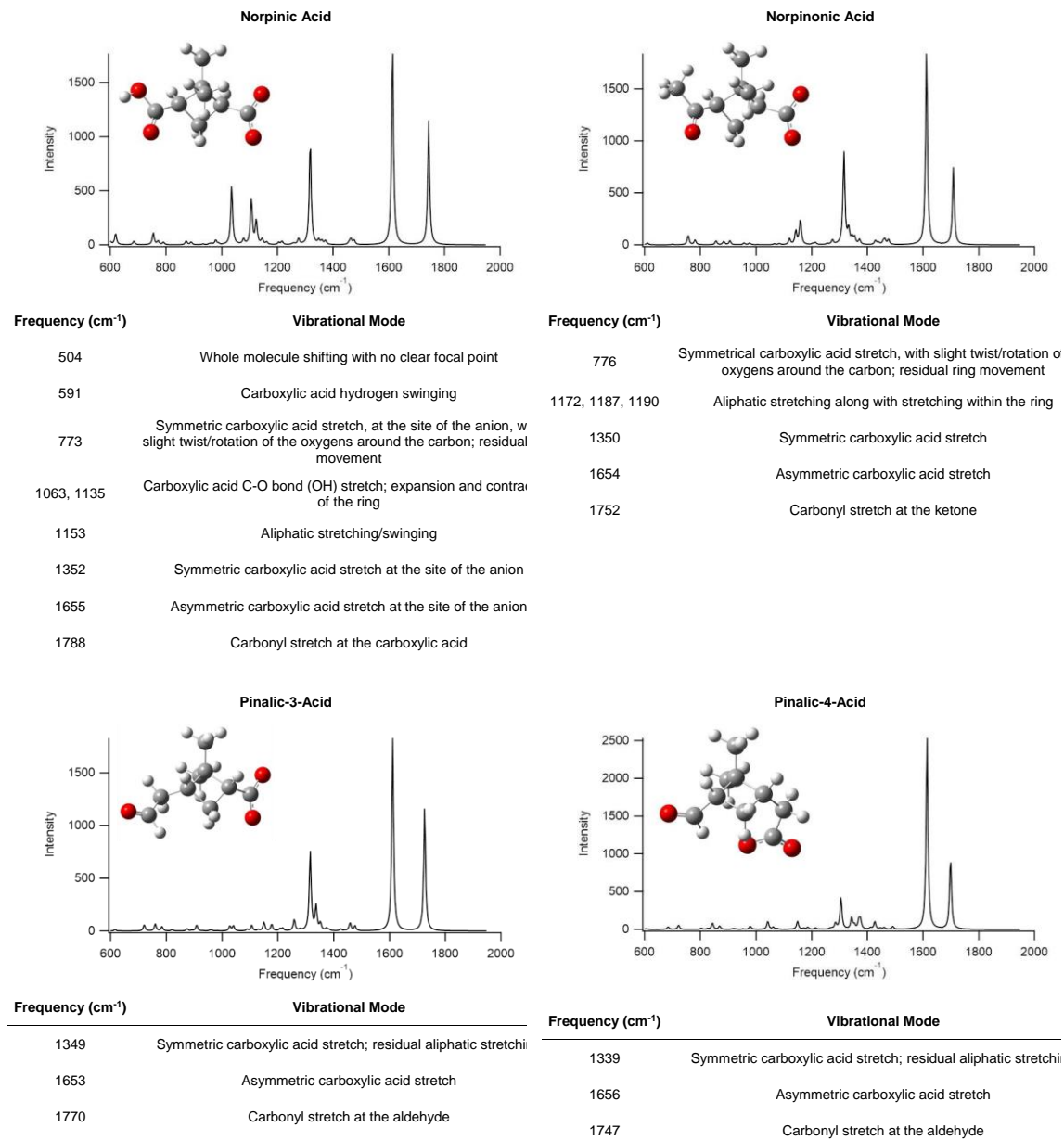
The laboratory will continue analyzing the composition and reactivity of deposited organic materials on indoor and outdoor surfaces. It is anticipated that laboratory aging experiments will take place in two different types of indoor chambers. The first will be a Teflon-film-lined chamber for surface water droplets with a temperature-controlled Teflon, multiwell plate, involving the photolysis box. Light will be directed into the box containing dew samples, where they will be irradiated and dried out simultaneously to see if and how composition changes. The second chamber will be a Teflon-lined glove box to enable time resolved, dry surface analysis. This dew analysis research, though in its beginning stages, lays the groundwork for an experimental platform to inform future research seeking to

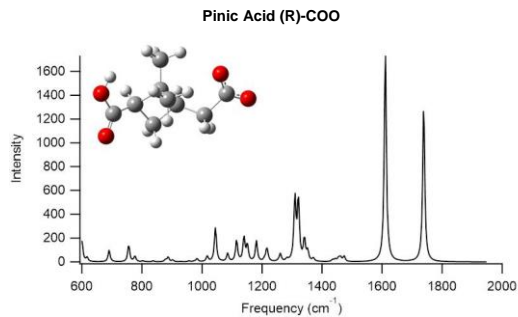
understand chemical transport and air quality through the study of aging organic films on natural surfaces.

This laboratory's ultimate goal with its research is to characterize chemical composition and changes as a result of atmospheric aging to understand carbon cycling, lifetimes, and transportation to improve existing atmospheric models and predictions benefitting human health and influence positive climate change.

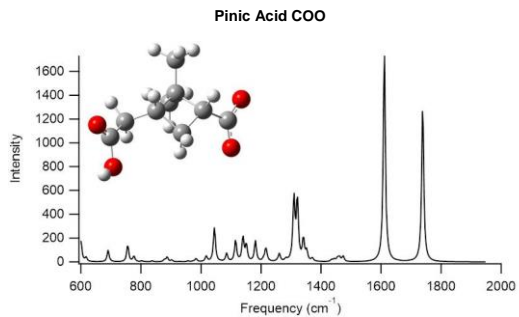
## APPENDIX A

**Table A1:** A summary of IR stretches for the lowest energy conformations of calculated anions.

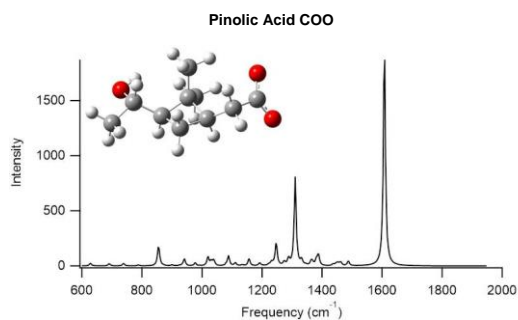




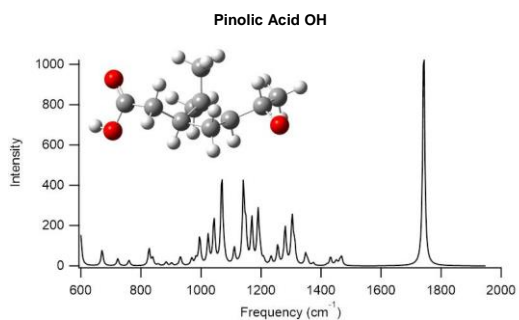
Frequency (cm <sup>-1</sup> )	Vibrational Mode
534	Carboxylic acid hydrogen swinging
1292	Carboxylic acid hydrogen swinging directly under carbon o carbonyl
1344	Symmetric carboxylic acid stretch at the site of the anion
1652	Asymmetric carboxylic acid stretch at the site of the anion
1822	Carbonyl stretch at the carboxylic acid (not at the site of the ar



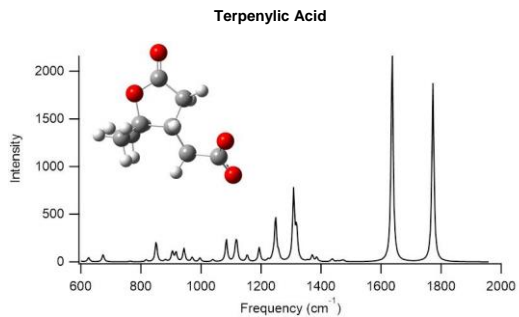
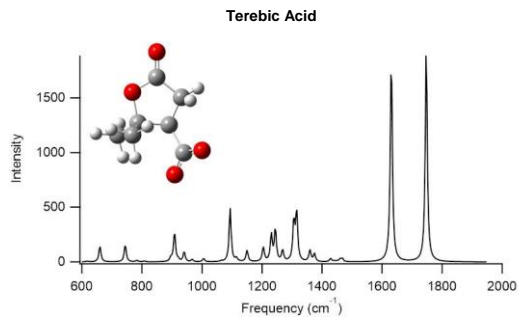
Frequency (cm <sup>-1</sup> )	Vibrational Mode
573	Carboxylic acid hydrogen swinging
584	Whole molecule shifting with no clear focal point
615	Carboxylic acid hydrogen swinging
1343	Symmetric carboxylic acid stretch at the site of the anion
1652	Asymmetric carboxylic acid stretch at the site of the anion
1783	Carbonyl stretch at the carboxylic acid (not at the site of the ar



Frequency (cm <sup>-1</sup> )	Vibrational Mode
1279	Alcohol hydrogen swinging
1344	Symmetric carboxylic acid stretch at the site of the anion
1649	Asymmetrical carboxylic acid stretch



Frequency (cm <sup>-1</sup> )	Vibrational Mode
567	Carboxylic acid hydrogen swinging
603	Hydrogen and carbonyl oxygen pinched towards each other a carboxylic acid
615	Carboxylic acid hydrogen swinging
1097, 1170	Rotation of hydrogens and carbons throughout the molecule : ring expansion and contraction
1787	Carbonyl stretch at the carboxylic acid



Frequency (cm <sup>-1</sup> )	Vibrational Mode
677, 931.71	Slight symmetric carboxylic acid stretch, but mainly a result of expansion and contraction of the 5-membered ring (latter more asymmetrical stretching within ring, focused around the oxygen contained within the ring)
763	Symmetric and slight twisting carboxylic acid stretch; expansion and contraction of the 5-membered ring
1349	Symmetric carboxylic acid stretch
1673	Asymmetric carboxylic acid stretch
1792	Carbonyl stretch not at the site of the anion

Frequency (cm <sup>-1</sup> )	Vibrational Mode
868, 1335	Symmetric carboxylic acid stretch
1670	Asymmetric carboxylic acid stretch
1809	Carbonyl stretch not at the site of the anion

## APPENDIX B

The xenon arc lamp uses a 299 nm cut-off filter. Solar radiation that reaches Earth's surface is greater than 290 nm, therefore light with shorter wavelengths is being absorbed and removed by the ozone layer. The cut-off filter implements the same principle as the ozone layer by removing this light from the lamp beam to produce a better match to ambient light. The lamp also had cooling water flow to limit IR exposure to the filters. IR light in the form of heat is coming from the lamp. To avoid the SOA film being heated, and thus evaporated, this water flow absorbs the IR light.

**Table B1:** A summary of the preliminary SOA sample filters. Filter name refers to the date SOA was loaded onto the filter with “a” designating a morning collection, “p” an afternoon collection, and “n” a night collection. Filters 10/22/18p and 10/23/18a were placed in the miniaturized chamber box without zero air flow or a Teflon cover. Filter 10/24/18p was placed in the box without zero air flow but with a Teflon cover.

Filter Name	SOA Mass (mg)*	SOA Loading Time	Irradiation Time	IR	UV/Vis
Blank	307.6**	—	—	Y	Y
10/22/18p	2.5	3hr	0hr	Y	N
			6hr		
			12hr		
			24hr		
			29hr		
10/23/18a	2.0	3hr	0hr	Y	N
			3hr		
			6hr		
			9hr		
			12hr		
10/24/18a	1.7	3hr	—	N	Y
10/24/18p	1.6	3hr	24hr	N	Y
10/25/18p	2.5	3hr	—	N	Y
11/1/18p	3.7	3hr	—	Y	N
11/2/18a	2.4	3hr	—	Y	N

\*Gravimetric; measured on a Denver Instrument APX – 200, d = 0.1 mg balance

\*\*Average mass of Zefluor filter

**Table B2:** The total sample volume ( $\mu\text{L}$ ) of dilutions for the UV/Vis analyzed box samples.

Dilution Step	Box 1.1	Box 1.2	Box 1.3	Box 1.4	Box 2.1-3	Box 2.4	Box 3	Box 4	Box 5
	180	180	180	180	180	180	180	180	180
120	300	300	300	300	300	300	300	300	300
100	400	400	400	400	400	400	400	400	400
100	500	500	500	500	500	500	500	500	500
100	600	600	600	600	600	600	600	600	600
100	700	700	700	700	700	700	700	700	700
150	850	850	850	850	850	850	850	850	850
150	1000	1000	1000	1000	1000	1000	1000	1000	1000
150	1150	1150	1150	1150	1150	1150	1150	1150	1150
200	1350	1350	1350	1350	1350	1350	1350	1350	1350
200	1550	1550	1550	1550	1550	1550	1550	1550	1550
200	1750	1750	1750	1750	1750	1750	1750	1750	1750
200	1950	1950	1950	1950	1950	1950	1950	1950	1950
300	2250	2250	2250	2250	2250	2250	2250	2250	2250
300	2550	2550	2550	2550	2550	2550	2550	2550	2550
300	2850	2850	2850	2850	2850	2850	2850	2850	2850
300	3150	3150	3150	3150	3150	3150	3150	3150	3150
300	3450	3450	3450	3450	3450	3450	3450	3450	3450

**Table B3:** A summary of SOA loaded, Zefluor filters photolyzed in the miniature chamber box under zero air flow and Teflon cover conditions. Extracted concentrations refers to AMS (g/L) and Orbitrap (mM) concentrations at a total sample volume of 180  $\mu\text{L}$ . Concentration data only concluded for Box 1 and thus extrapolated for Boxes 2 – 4.

	Filter Name	Box Starting Date	SOA Mass (mg)*	SOA Loading Time	Irradiation Time	Extracted Concentrations (g/L, mM)	
Box 1.1	10/30/18a	11/15/18	3.7	3hr	24hr	16.08	45.94
Box 1.2	10/29/18a		2.3	3hr	48hr	7.93	21.73
Box 1.3	10/26/18a		5.6	3hr	72hr	10.70	29.48
Box 1.4	10/29/18p		2.0	3hr	96hr	4.13	11.38
Box 2.1	10/30/18p	11/25/18	2.9	3hr	24hr	16.08	42.43
Box 2.2	10/31/18a		2.3	3hr	48hr	7.93	20.49
Box 2.3	10/31/18p		2.7	3hr	72hr	10.70	29.32
Box 2.4	11/1/18a		1.9	3hr	96hr	4.13	11.32
Box 3.1	11/3/18p	11/30/18	4.0	3hr	24hr	16.08	40.92
Box 3.2	11/3/18n		3.4	3hr	48hr	7.93	20.18
Box 3.3	11/5/18a		3.2	3hr	72hr	10.70	27.23
Box 3.4	11/6/18a		3.1	3hr	96hr	4.13	10.51
Box 4.1	11/7/18a	1/2/19	2.1	3hr	96hr	4.13	11.32
Box 4.2	11/7/18p		3.2	3hr	96hr	4.13	11.32
Box 4.3	11/8/18a		3.6	3hr	96hr	4.13	11.32
Box 4.4	11/13/18a		3.6	3hr	96hr	4.13	11.32

\*Gravimetric; measured on a Denver Instrument APX – 200, d = 0.1 mg balance

**Table B4:** A summary of SOA loaded, EZFlow filters photolyzed in the miniature chamber box under zero air flow and Teflon cover conditions. Box 5 consists of non-SOA loaded filters, subject to the box conditions but not exposed to light. Concentration data collection from the AMS and Orbitrap has not been conducted at this time.

	<b>Filter Name</b>	<b>Box Starting Date</b>	<b>SOA Mass (mg)*</b>	<b>SOA Loading Time</b>	<b>Irradiation Time</b>
	Blank		133.6**	—	—
<b>Box 5.1</b>	Dark 1	1/9/19	133.6**	—	96hr Dark
<b>Box 5.2</b>	Dark 2		133.6**	—	120hr Dark
<b>Box 5.3</b>	Dark 3		133.6**	—	144hr Dark
<b>Box 5.4</b>	Dark 4		133.6**	—	168hr Dark
<b>Box 6.1</b>	1/14/19a	1/25/19	1.1	3hr	120hr
<b>Box 6.2</b>	1/15/19a		0.6	3hr	144hr

\*Gravimetric; measured on a Denver Instrument APX – 200, d = 0.1 mg balance

\*\*Average mass of EZFlow filter

**Table B5:** An example, using Box 1.1, of the concentration calculations to create calibration curves.

Total Sample Volume ( $\mu\text{L}$ )	Concentration (g/L)	Molarity (mol/L)	molecules/L
180	16.08	0.0459	—
300	9.65	0.0276	1.7e19
400	7.24	0.0207	1.2e19
500	5.79	0.0165	10.0e18
...	...	...	...
3450	0.84	0.0024	1.4e18

The original AMS concentration is divided by the total sample volume of a dilution to get that dilution's concentration.

$$16.08 \frac{\text{g}}{\text{L}} (180 \mu\text{L}) / 300 \mu\text{L} = 9.65 \frac{\text{g}}{\text{L}}$$

This concentration is then divided by the mass obtained from the Orbitrap to convert into molarity.

$$9.65 \frac{\text{g}}{\text{L}} / 350 \frac{\text{g}}{\text{mol}} = 0.0276 \frac{\text{mol}}{\text{L}}$$

Then, molarity is converted into molecules per milliliter by multiplying molarity by Avogadro's number and dividing by milliliters.

$$0.0276 \frac{\text{mol}}{\text{L}} \left( 6.022 * 10^{23} \frac{\text{molecules}}{\text{mol}} \right) / 1000 \text{mL} = 1.7 * 10^{19} \frac{\text{molecules}}{\text{mL}}$$

**Table B6:** A summary of the IR stretches associated with this thesis.

Frequency (cm <sup>-1</sup> )	Absorption (cm <sup>-1</sup> )	Appearance	Group	Compound Class
4000 – 3000	3550 – 3200	Strong, Broad	O–H Stretch	Alcohol
3000 – 2500	3100 – 3000	Medium	C–H Stretch	Alkene
	3000 – 2840	Medium	C–H Stretch	Alkane
2000 – 1650	1750 – 1735	Strong	C=O Stretch	Lactone
	1720 - 1706	Strong	C=O Stretch	Carboxylic Acid of Dimer
1400 – 1000	1400 – 1000 1211, 1154 <sup>87</sup>	Strong	C–F Stretch	Fluoro Compound
<650	639 <sup>87</sup>	Strong	C–F Stretch	Fluoro Compound

IR Spectrum Table & Chart. Sigma-Aldrich<sup>88</sup>**Table B7:** A summary of the area of each fitted peak, as well as the percentage of the total area that peak accounts for, for Box 1.2, 3 and Box 3.2, 3.

48hr Light	Frequency (cm <sup>-1</sup> )	Area	Area Sum	% of Area
Peak 0	1641.5	1.6307	15.1005	10.8
Peak 1	1708	6.7362		44.6
Peak 2	1735.1	3.9043		25.9
Peak 3	1770.3	2.8293		18.7
<b>72hr Light</b>				
Peak 0	1641.5	2.7606	22.9897	12.0
Peak 1	1708	10.781		46.9
Peak 2	1735.1	5.0351		21.9
Peak 3	1770.3	4.4130		19.2
<b>48hr Dark</b>				
Peak 0	1641.5	0.80416	5.78165	13.9
Peak 1	1708	3.5997		62.3
Peak 2	1735.1	0.68852		11.9
Peak 3	1770.3	0.68927		11.9
<b>72hr Dark</b>				
Peak 0	1641.5	1.4754	11.9301	12.4
Peak 1	1708	7.4104		62.1
Peak 2	1735.1	1.5648		13.1
Peak 3	1770.3	1.4795		12.4

## APPENDIX C

### Abbreviations

AMS	Aerosol Mass Spectrometer
ATR-FTIR	Attenuated Total Reflectance Fourier Transform Infrared (Spectrometer)
CCN	Cloud Condensation Nuclei
DFT	Density Functional Theory
ESI	Electrospray Ionization
FEL	Free Electron Laser
FTICR	Fourier Transform Ion Cyclotron Resonance (Mass Spectrometer)
GC	Gas Chromatography
HR-TOF	High Resolution Time of Flight
IR	Infrared
IRMPD	Infrared Multiphoton Dissociation
MS	Mass Spectrometry/Spectrometer
POA	Primary Organic Aerosol
ROC	Reactive Organic Carbon
SOA	Secondary Organic Aerosol
SPE	Solid Phase Extraction
UHR-MS	Ultrahigh Resolution Mass Spectrometer
VOC	Volatile Organic Compound

## REFERENCES

1. Epstein, S.A.; Blair, S.L.; Nizkorodov, S.A. *Environ. Sci. Technol.*, **2014**, *48*, 11251 – 11258.
2. Henry, K.M.; Donahue, N.M. *J. Phys. Chem. A*, **2012**, *116*, 5932 – 5940
3. Hodzic, A.; Madronich, S.; Kasibhatla, P.S.; Tyndall, G.; Aumont, B.; Jimenez, J.L.; Lee-Taylor, J.; Orlando, J. *Atmos. Chem. Phys.*, **2015**, *15*, 9253 – 9269.
4. Kroll, J.H.; Ng, N.L.; Murphy, S.M.; Flagan, R.C.; Seinfeld, J.H. *Environ. Sci. Technol.*, **2006**, *15*, 1869 – 1877.
5. Wong, J.P.S.; Zhou, S.; Abbatt, J.P.D. *J. Phys. Chem. A*, **2015**, *119*, 4309 – 4316.
6. O'Brien, R.E.; Ridley, K.J.; Canagaratna, M.R.; Jayne, J.T.; Croteau, P.L.; Worsnop, D.R.; Budisulistiorini, S.H.; Surratt, J.D.; Follett, C.L.; Repeta, D.J.; Kroll, J.H. *Atmos. Meas. Tech. Discuss*, **2018**, in review.
7. Breitenlechner, M.; Fischer, L.; Hainer, M.; Heinritzi, M.; Curtius, J.; Hansel, A. *Anal. Chem.*, **2017**, *89*, 5824 – 5831.
8. Glasius, M.; Goldstein, A.H. *Environ. Sci. Technol.*, **2016**, *50*, 2754 – 2764.
9. Safieddine, S.; Heald, C.L. "Wet Deposition Flux of reactive Organic Carbon." *AGU*, **2016**.
10. Marley, N.A.; Gaffney, J.S. *ACS Symposium Series*, **2006**, 1 – 21.
11. Penner, J.E.; Andreae, M.; Annegarn, H.; Barrie, L.; Feichter, J.; Hegg, D.; Jayaraman, A.; Leaitch, R.; Murphy, D.; Nganga, J.; Pitari, G. *IPCC WG1 Third Assessment Report*, **2000**, 289 – 348.
12. Prentice, I.C.; Farquhar, G.D.; Fasham, M.J.R.; Goulden, M.L.; Heimann, M.; Jaramillo, V.J.; Kheshgi, H.S.; LeQuéré, C.; Scholes, R.J.; Wallace, D.W.R. IPCC, 2001: *Climate Change 2001: The Scientific Basis. Contributions of Working Group I to the Third Assessment Report of the Intergovernmental Panel on Climate Change*. Cambridge University Press, Cambridge, United Kingdom and New York, NY, USA, 185 – 237.
13. Voiland, A. "Aerosols: Tiny Particles, Big Impact." NASA, NASA, **2010**. [earthobservatory.nasa.gov/features/Aerosols/page1.php](http://earthobservatory.nasa.gov/features/Aerosols/page1.php)
14. Hallquist, M.; Wenger, J.C.; Baltensperger, U.; Rudich, Y.; Simpson, D.; Claeys, M.; Dommen, J.; Donahue, N.M.; George, C.; Goldstein, A.H.; Hamilton, J.F.; Herrmann, H.; Hoffmann, T.; Iinuma, Y.; Jang, M.; Jenkin, M.E.; Jimenez, J.L.; Kiendler-Scharr, A.; Maenhaut, W.; McFiggans, G.; Mentel, Th.F.; Monod, A.; Prevot, A.S.H.; Seinfeld, J.H.; Surratt, J.D.; Szmigielski, R.; Wildt, J. *Atmos. Chem. Phys.*, **2009**, *9*, 5155 – 5236.

15. Kommalapati, R.R.; Valsaraj, K.T. Atmospheric aerosols and their importance. *ACS Symposium Series*, **2009**, 1 – 10.
16. Jacob, D.J. *Introduction to Atmospheric Chemistry*. Princeton University Press, **1999**.
17. O'Brien, R.E. Chemical characterization of organic compounds in dew water. **2017**, 1 – 4.
18. O'Brien, R.E.; Neu, A.; Epstein, S.A.; MacMillan, A.C.; Wang, B.; Kelly, S.T.; Nizkorodov, S.A.; Laskin, A.; Moffet, R.C.; Gilles, M.K. *Geophys. Res. Lett.*, **2014**, *41*, 4347 – 4353.
19. Zhang, Q.; Jimenez, J.L.; Canagaratna, M.R.; Allan, J.D.; Coe, H.; Ulbrich, I.; Alfarra, M.R.; Takami, A.; Middlebrook, A.M.; Sun, Y.L.; Dzepina, K.; Dunlea, E.; Docherty, K.; DeCarlo, P.F.; Salcedo, D.; Onasch, T.; Jayne, J.T.; Miyoshi, T.; Shimojo, A.; Hatakeyama, S.; Takegawa, N.; Kondo, Y.; Schneider, J.; Drewnick, F.; Borrmann, S.; Weimer, S.; Demerjian, K.; Williams, P.; Bower, K.; Bahreini, R.; Cottrell, L.; Griffin, R.J.; Rautiainen, J.; Sun, J.Y.; Zhang, Y.M.; Worsnop, D.R. *Geophys. Res. Lett.*, **2007**, *34*, L13801.
20. O'Brien, R.E.; Nguyen, T.B.; Laskin, A.; Laskin, J.; Hayes, P.L.; Liu, S.; Jimenez, J.L.; Russell, L.M.; Nizkorodov, S.A.; Goldstein, A.H. *J. Geophys. Res. Atmos.*, **2013**, *118*, 1042 – 1051.
21. Vaden, T.D.; Imre, D.; Beránek, J.; Shrivastava, M.; Zelenyuk, A. *Proc. Natl. Acad. Sci. U.S.A.*, **2011**, *108*, 2190 – 2195.
22. Virtanen, A.; Joutsensaari, J.; Koop, T.; Kannosto, J.; Yli-Pirilä, P.; Leskinen, J.; Mäkelä, J.M.; Holopainen, J.K.; Pöschl, U.; Kulmala, M.; Worsnop, D.R.; Laaksonen, A. *Nature*, **2010**, *467*, 824 – 827.
23. Lagzi, I.; Mészáros, R.; Gelybó, G.; Leelőssy, A. *Atmospheric Chemistry*. Eötvös Loránd University, **2013**.
24. Speight, J.G. *Environmental Organic Chemistry for Engineers*. Elsevier Inc., **2016**.
25. Oliveira, B.F.; Ignotti, E.; Hacon, S.S. *Cad Saude Publica*, **2011**, *9*, 1678 – 1698.
26. Pöschl, U. *Angew. Chem. Int. Ed.*, **2005**, *44*, 7520 – 7540.
27. Safieddine, S.A.; Heald, C.L.; Henderson, B.H. *Geophys. Res. Lett.*, **2017**, *44*, 3897 – 3906.
28. Hansen, J.; Sato, M.; Ruedy, R.; Nazarenko, L.; Lacis, A.; Schmidt, G.A.; Russell, G.; Aleinov, I.; Bauer, M.; Bauer, S.; Bell, N.; Cairns, B.; Canuto, V.; Chandler, M.; Cheng, Y.; Del Genio, A.; Faluvegi, G.; Fleming, E.; Friend, A.; Hall, T.; Jackman, C.; Kelley, M.; Kiang, N.; Koch, D.; Lean, J.; Lerner, J.; Lo, K.; Menon, S.; Miller, R.; Minnis, P.; Novakov, T.; Oinas, V.; Perlwitz, Ja.; Perlwitz, Ju.; Rind, D.; Romanou, A.; Shindell, D.; Stone, P.;

- Sun, S.; Tausnev, N.; Thresher, D.; Weilicki, B.; Wong, T.; Yao, M.; Zhang, S. Efficacy of climate forcings. *J. Geophys. Res.*, **2005**, *110*, 1 – 45.
29. Winterhalter, R.; Van Dingenen, R.; Larsen, B.R.; Jensen, N.R.; Hjorth, J. *Atmos. Chem. Phys. Discuss.*, **2003**, *3*, 1 – 39.
30. “Climate Change Indicators: Climate Forcing.” *U.S. Environ. Protection Agency, EPA*, **2016**, [epa.gov/climate-indicators/climate-change-indicators-climate-forcing](http://epa.gov/climate-indicators/climate-change-indicators-climate-forcing)
31. Charlson, R.J.; Schwartz, S.E.; Hales, J.M.; Cess, R.D.; Coakley Jr., J.A.; Hansen, J.E.; Hofmann, D.J. *Science*, **1992**, *255*, 423 – 430.
32. Kanakidou, M.; Seinfeld, J.H.; Pandis, S.N.; Barnes, I.; Dentener, F.J.; Facchini, M.C.; Van Dingenen, R.; Ervens, B.; Nenes, A.; Nielsen, C.J.; Swietlicki, E.; Putaud, J.P.; Balkanski, Y.; Fuzzi, S.; Horth, J.; Moortgat, G.K.; Winterhalter, R.; Myhre, C.E.L.; Tsigaridis, K.; Vignati, E.; Stephanou, E.G.; Wilson, J. *Atmos. Chem. Phys.*, **2005**, *5*, 1053 – 1123.
33. Houghton, J.T.; Ding, Y.; Griggs, D.J.; Noguer, M.; van der Linden, P.J.; Dai, X.; Maskell, K.; Johnson, C.A. IPCC, 2001: *Climate Change 2001: The Scientific Basis. Contribution of Working Group I to the Third Assessment Report of the Intergovernmental Panel on Climate Change*. Cambridge University Press, Cambridge, United Kingdom and New York, NY, USA, 881.
34. “Scientific Consensus: Earth’s Climate is Warming.” *NASA, NASA*, [climate.nasa.gov/scientific-consensus](http://climate.nasa.gov/scientific-consensus)
35. Monroe, R. “The History of the Keeling Curve.” *SCRIPPS Institute of Oceanography*, **2013**, [scripps.ucsd.edu/programs/keelingcurve/2013/04/03/the-history-of-the-keeling-curve](http://scripps.ucsd.edu/programs/keelingcurve/2013/04/03/the-history-of-the-keeling-curve)
36. Keeling, R.F.; Piper, S.C.; Bollenbacher, A.F.; Walker J.S. **2009**.
37. Keeling, R.F.; Manning, A.C. In *Treatise on Geochemistry*, 2<sup>nd</sup> ed.; **2018**, 385 – 404.
38. *Inventory of U.S. Greenhouse Gas Emissions and Sinks. U.S. Environ. Protection Agency, EPA*, **1990 – 2015**.
39. de Gouw, J.A.; Jimenez, J.L. *Environ. Sci. Technol.*, **2009**, *43*, 7614 – 7618.
40. de Gouw, J.A.; Middlebrook, A.M.; Warneke, C.; Goldan, P.D.; Kuster, W.C.; Roberts, J.M.; Fehsenfeld, F.C.; Worsnop, D.R.; Canagaratna, M.R.; Pszenny, A.A.P.; Keene, W.C.; Marchewka, M.; Bertman, S.B.; Bates, T.S. *J. Geophys. Res. Atmos.*, **2005**, *110*, D16305.
41. Pankow, J. F. *Atmos. Environ.*, **1994**, *28*, 189 – 193.

42. Jimenez, J.L.; Canagaratna, M.R.; Donahue, N.M.; Prévôt, A.S.H.; Zhang, Q.; Kroll, J.H.; DeCarlo, P.F.; Allan, J.D.; et al. *Science*, **2009**, 326, 1525 – 1529.
43. Vaden, T.D.; Song, C.; Rahul, A.Z.; Imre, D.; Zelenyuk, A. *Proc. Natl. Acad. Sci. U.S.A.*, **2010**, 107, 6658 – 6663.
44. O'Brien, R.E.; Laskin, A.; Laskin, J.; Rubitschun, C.L.; Surratt, J.D.; Goldstein, A.H. *J. Geophys. Res. Atmos.*, **2014**, 119, 706 – 12, 720.
45. O'Brien, R.E.; Laskin, A.; Laskin, J.; Liu, S.; Weber, R.; Russell, L.M.; Goldstein, A.H. *Atmos. Environ.*, **2013**, 68, 265 – 272.
46. Lin, P.; Fleming, L.T.; Nizkorodov, S.A.; Laskin, A.; Laskin, J. *Anal. Chem.*, **2018**, 15, 12.
47. Nguyen, T.B.; Lee, P.B.; Updyke, K.M.; Bones, D.L.; Laskin, A.; Laskin, J.; Nizkorodov, S.A. *J. Geophys. Res. Atmos.*, **2012**, 117, (D1).
48. Pratt, K.A.; Prather, K.A. *Mass Spectrom. Rev.*, **2012**, 31, 1 – 48.
49. Isaacman-Vanwertz, G.; Massoli, P.; O'Brien, R.E.; Lim, C.; Franklin, J.P.; Moss, J.A.; Hunter, J.F.; Nowak, J.B.; Canagaratna, M.R.; Misztal, P.K.; et al. *Nat. Chem.*, **2018**, 10, 462 – 468.
50. Laskin, J.; Laskin, A.; Nizkorodov, S.A. *Anal. Chem.*, **2017**, 90, 166 – 189.
51. Isaacman, G.; Kreisberg, N.M.; Yee, L.D.; Worton, D.R.; Chan, A.W.H.; Moss, J.A.; Hering, S.V.; Goldstein, A.H. *Atmos. Meas. Tech.*, **2014**, 7, 4417 – 4429.
52. Isaacman-Vanwertz, G.; Yee, L.D.; Kreisberg, N.M.; Wernis, R.; Moss, J.A.; Hering, S.V.; de Sá, S.S.; Martin, S.T.; Alexander, M.L.; Palm, B.B.; Hu, W.; Campuzano-Jost, P.; Day, D.A.; Jimenez, J.L.; Riva, M.; Surratt, J.D.; Viegas, J.; Manzi, A.; Edgerton, E.; Baumann, K.; Souza, R.; Artaxo, P.; Goldstein, A.H. *Environ. Sci. Technol.*, **2016**, 50, 9952 – 9962.
53. Worton, D.R.; Decker, M.; Isaacman-Vanwertz, G.; Chan, A.W.H.; Wilson, K.R.; Goldstein, A.H. *Analyst.*, **2017**, 142, 2395 – 2403.
54. Cui, T.; Zeng, Z.; dos Santos, E.O.; Zhang, Z.; Chen, Y.; Zhang, Y.; Rose, C.A.; Budisulistiorini, S.H.; Collins, L.B.; Bodnar, W.M.; de Souza, R.A.F.; Martin, S.T.; Machado, C.M.D.; Turpin, B.J.; Gold, A.; Ault, A.P.; Surratt, J.D. *Environ. Sci. Process. Impacts*, **2018**, 20, 1524 – 1536.
55. Krechmer, J.E.; Groessl, M.; Zhang, X.; Junninen, H.; Massoli, P.; Lambe, A.T.; Kimmel, J.R.; Cubison, M.J.; Graf, S.; Lin, Y.H.; et al. *Atmos. Meas. Tech.*, **2016**, 9, 3245 – 3262.
56. Sancar, A. *Adv. Protein Chem.*, **2004**, 69, 73 – 100.
57. Bhutani, V.K.; Lamola, A.A. *Fetal and Neonatal Physiology (5<sup>th</sup>. Ed.)*, **2017**, 2, 942 – 952.
58. *FELIX Laboratory*, Radboud University, **2019**, ru.nl/felix/

59. O'Brien, J.T.; Prell, J.S.; Steill, J.D.; Oomens, J.; Williams, E.R. *J. Phys. Chem. A*, **2008**, *112*, 10823 – 10830.
60. Forbes, M.W.; Bush, M.F.; Polfer, N.C.; Oomens, J.; Dunbar, R.C.; Williams, E.R.; Jockusch, R.A. *J. Phys. Chem. A*, **2007**, *111*, 11759 – 11770.
61. Martens, J.; Grzetic, J.; Berden, G.; Oomens, J. *Nat. Commun.* **2016**, *7*, 11754.
62. Martens, J.; Berden, G.; Bentlage, H.; Coene, K.L.M.; Engelke, U.F.; Wishart, D.; van Scherpenzeel, M.; Kluijtmans, L.A.J.; Wevers, R.A.; Oomens, J. *J. Inherit. Metab. Dis.*, **2018**, *41*, 367 – 377.
63. Prell, J.S.; Chang, T.M.; O'Brien, J.T.; Williams, E.R. *J. Am. Chem. Soc.*, **2010**, *132*, 7811 – 7819.
64. Poutsma, J.C.; Martens, J.; Oomens, J.; Maitre, P.; Steinmetz, V.; Bernier, M.; Jia, M.; Wysocki, V. *J. Am. Soc. Mass Spectrom.*, **2017**, *28*, 1482 – 1488.
65. Frisch, M.J.; Trucks, G.W.; Schlegel, H.B.; Scuseria, G.E.; Robb, M.A.; Cheeseman, J.R.; Scalmani, G.; Barone, V.; Mennucci, B.; Petersson, G.A.; Nakatsuji, H.; Caricato, M.; Li, X.; Hratchian, H.P.; Izmaylov, A.F.; Bloino, J.; Zheng, G.; Sonnenber, D.J. *Gaussian 09. Gaussian, Inc. Wallingford CT.* **2009**.
66. Heiles, S.; Cooper, R.J.; Berden, G.; Oomens, J.; Williams, E.R. *Phys. Chem. Chem. Phys.*, **2015**, *17*, 30642 – 30647.
67. Oomens, J.; Steill, J.D.; Redlich, B. *J. Am. Chem. Soc.*, **2009**, *131*, 4310 – 4319.
68. Kalberer, M.; Paulsen, D.; Sax, M.; Steinbacher, M.; Dommen, J.; Prevot, A.S.H.; Fisseha, R.; Weingartner, E.; Frankevich, V.; Zenobi, R.; et al. *Science*, **2004**, *303*, 1659 – 1662.
69. Tolocka, M.P.; Jang, M.; Ginter, J.M.; Coz, F.J.; Kamens, R.M.; Johnston, M.V. *Environ. Sci. Technol.*, **2004**, *38*, 1428 – 1434.
70. Silverstein, R.M.; Webster, F.X.; Kiemle, D.J. *Spectrometric Identification of Organic Compounds* Seventh Edition. John Wiley Sons, Inc., **2005**.
71. Zhang, X.; McVay, R.C.; Huang, D.D.; Dalleska, N.F.; Aumont, B.; Flagan, R.C.; Seinfeld, J.H. *Proc. Natl. Acad. Sci. U.S.A.*, **2015**, *112*, 14168 – 14173.
72. Finessi, E.; Lidster, R.T.; Whiting, F.; Elliott, T.; Alfarra, M.R.; Mcfiggans, G.B.; Hamilton, J.F. *Anal. Chem.*, **2014**, *86*, 11238 – 11245.
73. Bythell, B.J.; Rabus, J.M.; Wagoner, A.R.; Abutokaikah, M.T.; Maître, P. *J. Am. Soc. Mass Spectrom.*, **2018**, *29*, 2380 – 2393.

74. Yasmeen, F.; Szmigielski, R.; Vermeylen, R.; Gómez-González, Y.; Surratt, J.D.; Chan, A.W.H.; Seinfeld, J.H.; Maenhaut, W.; Claeys, M. *J. Mass Spectrom.*, **2011**, *46*, 425 – 442.
75. Claeys, M.; Iinuma, Y.; Szmigielski, R.; Surratt, J.D.; Blockhuys, F.; Alsenoy, C.V.; Boge, O.; Sierau, B.; Gomez-Gonzalez, Y.; Vermeylen, R.; et al. *Environ. Sci. Technol.*, **2009**, *43*, 6976 – 6982.
76. Jaoui, M.; Kamens, R.M. *J. Atmos. Chem.*, **2003**, *44*, 259 – 297.
77. Kroll, J.H.; Seinfeld, J.H. *Atmos. Environ.*, **2008**, *42*, 3593 – 3624.
78. Tkachenko, N. V. *Optical Spectroscopy: Methods and Instrumentations*. Institute of Materials Chemistry Tampere University of Technology, Tampere, Finland, **2006**.
79. Kuhn, H.J.; Braslavsky, S.E.; Schmidt, R. *Pure Appl. Chem.*, **2004**, *76*, 2105 – 2146.
80. Mang, S.A.; Henricksen, D.K.; Bateman, A.P.; Andersen, M.P.S.; Blake, D.R.; Nizkorodov, S.A. *J. Phys. Chem. A*, **2008**, *112*, 8337 – 8344.
81. Agam, N.; Berliner, P.R. *J. Arid Environ.*, **2006**, *65*, 572 – 590.
82. Stone, E.C. *Q. Rev. Biol.*, **1963**, *38*, 328 – 341.
83. Guide to Solid Phase Extraction. Sigma-Aldrich.
84. Hennion, M.C. *J. Chromatogr. A.*, **1999**, *856*, 3 – 54.
85. Singh, S. *Adv. Agron.*, **2014**, *128*, 97 – 135.
86. Schmitt-Kopplin, P.; Hertkorn, N. *Anal. Bioanal. Chem.*, **2007**, *5*, 1309 – 1310.
87. Fazullin, D.D.; Mavrin, G.V.; Sokolov, M.P.; Shaikhiev, I.G. *Modern Applied Science*, **2015**, *9*, 242 – 249.
88. IR Spectrum Table & Chart. Sigma-Aldrich. [sigmaaldrich.com/technical-documents/articles/biology/ir-spectrum-table](http://sigmaaldrich.com/technical-documents/articles/biology/ir-spectrum-table).